Daily estimates of aerosol optical thickness over land surface based on a directional and temporal analysis of SEVIRI MSG visible observations

Dominique Carrer, Jean-Louis Roujean, Olivier Hautecoeur, Thierry Elias

JOURNAL OF GEOPHYSICAL RESEARCH, VOL. 115, D10208, doi:10.1029/2009JD012272, 2010

Daily estimates of aerosol optical thickness over land surface based on a directional and temporal analysis of SEVIRI MSG visible observations

Dominique Carrer,[1] Jean-Louis Roujean,[1] Olivier Hautecoeur,[1] and Thierry Elias[2]

Received 17 April 2009; revised 20 November 2009; accepted 22 December 2009; published 25 May 2010.

[1] This paper presents an innovative method for obtaining a daily estimate of a quality-controlled aerosol optical thickness (AOT) of a vertical column of the atmosphere over the continents. Because properties of land surface are more stationary than the atmosphere, the temporal dimension is exploited for simultaneous retrieval of the surface and aerosol bidirectional reflectance distribution function (BRDF) coming from a kernel-driven reflectance model. Off-zenith geometry of illumination enhances the forward scattering peak of the aerosol, which improves the retrieval of AOT from the aerosol BRDF. The solution is obtained through an unconstrained linear inversion procedure and perpetuated in time using a Kalman filter. On the basis of numerical experiments using the 6S atmospheric code, the validity of the BRDF model is demonstrated. The application is carried out with data from the Spinning Enhanced Visible and Infra Red Imager (SEVIRI) instrument on board the geostationary Meteosat Second Generation (MSG) satellite from June 2005 to August 2007 for midlatitude regions and from March 2006 to June 2006 over desert sites. The satellite-derived SEVIRI AOT compares favorably with Aerosol Robotic Network (AERONET) measurements for a number of contrasted stations and also similar Moderate Resolution Imaging Spectroradiometer (MODIS) products, within 20% of relative accuracy. The method appears competitive for tracking anthropogenic aerosol emissions in the troposphere and shows a potential for the challenging estimate of dust events over bright targets. Moreover, a high-frequency distribution of AOT provides hints as to the variability of pollutants according to town density and, potentially, motor vehicle traffic. The outcomes of the present study are expected to promote a monitoring of the global distributions of natural and anthropogenic sources and sinks of aerosol, which are receiving increased attention because of their climatic implications.

Citation: Carrer, D., J.-L. Roujean, O. Hautecoeur, and T. Elias (2010), Daily estimates of aerosol optical thickness over land surface based on a directional and temporal analysis of SEVIRI MSG visible observations, *J. Geophys. Res.*, *115*, D10208, doi:10.1029/2009JD012272.

1. Introduction

[2] Aerosols affect the radiation balance of the Earth's atmosphere and have a potentially significant climate forcing effect. Therefore, the role of aerosols is crucial in projecting future climate scenarios [*Haywood and Boucher*, 2000]. Because atmospheric particles have a direct link with energy use, economic activities and societal impacts of climate change, the topic entails political issues in the context of the *Intergovernmental Panel on Climate Change* [2007]. A determination of the aerosol load in the low troposphere is at the core of many applications in a vast number of domains like epidemiologic risk, food security, air quality, health, hazard management, weather forecasting, climate change detection and the hydrological cycle [*Ramanathan et al.*, 2001; *Kaufman et al.*, 2002; *Tanré et al.*, 2005]. Aerosols essentially originate from human activities, dust storms, biomass burning, vegetation, the sea, volcanoes, and also from the gas-to-particle conversion mechanism. Large values of aerosol charge are due to direct anthropogenic impact, like transported polluted air masses. Another major contribution comes from dust from semiarid regions. A mixing of aerosol classes from different sources of emission is generally observed and the aerosols interact rapidly with trace gases and water, which leads to wet and dry deposition [*Reid and Hobbs*, 1998; *Anderson et al.*, 2003; *Haywood et al.*, 2003]. The intrinsic characteristics of aerosol classes combined with the surface reflectance

[1]GAME, CNRM, Météo-France, CNRS, Toulouse, France.
[2]LSCE, IPSL, Gif-sur-Yvette, France.

0148-0227/10/2009JD012272

magnitude determine whether the aerosol contributes to cooling or heating [*Satheesh*, 2002]. For instance, high aerosol scattering reduces the solar radiation reaching the ground and creates a cooling effect. In addition, a bright surface implies a positive aerosol forcing at the top of the atmosphere due to increased absorption of reflected radiation. Thus transport and sedimentation are key factors in the analysis of the heterogeneous distribution of aerosols.

[3] Aerosols are scatterers and absorbers of radiation that are heavily concentrated in the lowest portion of the atmosphere. They can also act as cloud condensation nuclei, thereby contributing to the formation of clouds and influencing their microphysics. The methods for investigating single scattering of spherical particles, or nonspherical particles of small size compared to wavelength, that are mutually independent are Mie theory [*Liou and Hansen*, 1971], and T matrix [*Mishchenko et al.*, 1996]. The case of nonspherical particles of large size is treated using ray tracing or Monte Carlo [*Kokhanovsky and Nakajima*, 1998], and geometric optics [*Zhou et al.*, 2003]. The properties of aerosols can be verified over selected regions through the Aerosol Robotic Network (AERONET), which encompasses hundreds of stations around the world, equipped with Sun-sky scanning spectral radiometers [*Holben et al.*, 1998]. But the scarcity of the ground network distribution is not favorable for the reconstruction of the global fields of aerosol by interpolation. This rather suggests the necessity for a synergistic use of the deployment of satellite sensors. An important requirement of the scientific community is to establish a global climatology of aerosols. For the past decade, it has been largely supported by the advent of several remote sensing programs to document the quantity and nature of the aerosol in a consistent manner on a global scale.

[4] The Polarization and Directionality of Earth Reflectance (POLDER) and Glory Aerosol Polarimetry Sensor (APS) sensors exploit the polarization, directionality and spectral properties of the signal [*Herman et al.*, 2005]. The Moderate Resolution Imaging Spectroradiometer (MODIS) is based on a multispectral approach [*Ichoku et al.*, 2005] while the Multiangle Imaging Spectroradiometer (MISR) takes advantage of the multiangular capabilities of the instrument [*Kahn et al.*, 2005]. The combination of the two has been found to be of added value [*Abdou et al.*, 2005]. Further, information at very short wavelengths has been exploited by projects like the Global Ozone Monitoring Experiment (GOME) [see *Kusmierczyk-Michulec and de Leeuw*, 2005] and the Sea-viewing Wide Field-of-view Sensor (SeaWiFS) [*Wang et al.*, 2005]. Long-term series of Advanced Very High Resolution Radiometer (AVHRR) data have been judged beneficial to assess climatologic trends in combination with MODIS data [*Jeong et al.*, 2005] or Total Ozone Mapping Spectrometer (TOMS) data [*Jeong and Li*, 2005].

[5] It is noteworthy that the instruments mentioned above were onboard polar orbiting systems and could provide a value of an aerosol load on the characteristic time scale of a day in the ideal situation. Therefore, such space missions cannot depict the day-to-day variations of aerosol presence when rapid changes occur in spatial patterns. So far, the algorithms developed for aerosol retrieval have exploited primarily the spectral and spatial dimension of the signal. An examination of the wavelength dependence provides information for an analysis of the aerosol mode (fine, medium, coarse), which can be completed by polarization measurements. This generally leads to the definition of light scattering phase functions. A useful parameter that quantifies the columnar amount of particles in the atmosphere is the aerosol optical thickness (AOT). An effective, widespread method for AOT retrieval is to consider dark targets such as inland water bodies and dense vegetation where most of the signal reaching a satellite sensor is contributed by the atmosphere at visible wavelengths. However, the majority of aerosol emissions arise from bright surfaces (desert, semi-arid areas). Also, AOT could be assessed on the basis of the visibility (visual) range to describe the haze level of the atmosphere due to aerosols.

[6] The main difficulty is to isolate the aerosol radiance in satellite measurements stems from an ambiguous separation of the light scattering signatures between the atmosphere and the adjacent land surface [e.g., *Sinyuk et al.*, 2007]. On the one hand, accurate knowledge of the magnitude and variations in surface albedo is mandatory, particularly over arid and semiarid regions, in order to retrieve aerosol properties from satellite and ground-based measurements [*Dubovik and King*, 2000]. On the other hand, the determination of a surface albedo is conditioned by the adequacy of the atmospheric intervention, which depends to a large extent to our knowledge of the aerosol properties. Because of this dilemma, a simultaneous inversion of surface and aerosol properties is advised in practice. Previous studies have demonstrated that the problem could be solved with data from the geostationary satellite Meteosat [*Pinty et al.*, 2000; *Knapp et al.*, 2005; *Elias and Roujean*, 2008]. Fast estimation of aerosol type information over land surfaces can be now envisaged with the Spinning Enhanced Visible and Infra Red Imager (SEVIRI) onboard the geostationary Earth observation system, Meteosat Second Generation (MSG). A conceivable method is to consider a multi-temporal approach to the critical surface defined as the surface reflectance where the measured top-of-atmosphere reflectance remains constant with variable aerosol concentration [*Popp et al.*, 2007]. A comparison with ground data reveals a dependable distinction between highly scattering and absorbing aerosol types but the algorithm is not yet operational for suggesting systematic assessment of the effect of aerosol absorption and scattering.

[7] In contrast with the preferred spectral-based and space-based methods, the method presented here focuses on a directional and temporal inspection of the satellite signal. The present method operates a simultaneous retrieval of the aerosol and surface bidirectional reflectance distribution function (BRDF). Aerosol and surface components are represented in a kernel-driven BRDF model allowing fast computations of surface albedo [*Roujean et al.*, 1992; *Wanner et al.*, 1995]. The geometric effects and the volume scattering constitute the two surface kernels. The backbone of the single scattering aerosol kernel is the semiphysical Henyey-Greenstein phase function previously considered to treat the optical radiation transfer for flat, thick natural media constituted of particles of any shape [*Mishchenko et al.*, 1999]. According to *Kokhanovsky et al.* [2005], this phase function can replace favorably Mie theory for practical application because the radiation terms are less sensitive to an accurate angular definition than to the asymmetry

factor. Owing to grazing illumination, the intensity and the width of the reflectance peak of aerosols is enhanced in the forward scattering direction. Since the characteristics of this angular signature are mostly driven by the size of particles, any aggregation process or change in size distribution will modify the properties of the aerosol peak [see *Boucher*, 1998]. This explains why the presence of aerosols modifies more rapidly the observed satellite reflectance in the forward direction than change that would affect the surface BRDF. By combining the directional and temporal dimensions of the satellite signal, it is possible to unravel the aerosol and surface components. The computation of the AOT is finally derived (see review by *Kokhanovsky and de Leeuw* [2009]). The BRDF solution is obtained through an unconstrained linear inversion procedure of a kernel-driven model [*Roujean et al.*, 1992]. We use a recursive procedure based on a Kalman filter to provide a quality-controlled BRDF product and a diurnally averaged AOT.

[8] We consider the clear-sky quarter-hourly scenes of the VIS06 (650 nm) band of the SEVIRI instrument, which ensures the geographic coverage for Europe, Africa, and the eastern part of South America with a subsatellite pixel resolution of 3 km [*Schmetz et al.*, 2002]. Data are routinely processed in near real time in the framework of the Satellite Application Facility (SAF) program on Land Surface Analyses (LSA) [e.g., *Trigo et al.*, 2010], referred to in the rest of the text as Land SAF. The objectives of the Land SAF program are to provide added value products for the meteorological and environmental science communities with applications in the fields of land surface modeling, hydrology, and climatology. The reliability of the method is appraised with respect to the retrieval of aerosols over desert regions, for which the high brightness of the surface means that a quantitative assessment of aerosols from the satellite radiometry is still a challenge [*Kaufman et al.*, 1997; *Remer et al.*, 2005]. The value of the asymmetry factor is fixed, somewhat arbitrarily, for small size particles because it is dominant over continents if we except Sahara region.

[9] Section 2 presents the physical assumptions and the synthetic theory underlying the BRDF kernel-driven approach for land surface targets, extended here to aerosols. The recursive method and model inversion are also presented. Accuracy of the algorithm is tested in section 3 with an observation system based on simulation experiment. Section 3 also presents maps of SEVIRI-derived AOT products over selected regions of Europe and Africa. An evaluation study is shown, based on in situ measurements from the AERONET network and comparison with the MODIS aerosol product. Section 4 presents an analysis of the errors due the necessary underlying physical assumptions in order to obtain a tractable and computationally efficient algorithmic system. Section 5 discusses the obtained results and stresses perspectives of application in an operational context.

2. Methodology

2.1. Theory and Physical Assumptions

[10] The linear theory on radiative transfer can advantageously replace more complex theories as it offers fast and robust solutions to operational problems. In the present work, we consider a vertical two-layer medium. The top layer is composed only of atmospheric particles. The signal impinging at the top of the aerosol layer is assumed to be free of gaseous absorption and Rayleigh scattering. The bottom layer is formed by the background surface. Hence, Top Of Layer (TOL) will be used to refer to the top of the aerosol layer in what follows. In this respect, the solution to the classical radiation transfer equation corresponding to a light beam traveling from the TOL level downward to a land surface pixel and being bounced back upward to this level reads [*Lenoble*, 1985]:

$$\rho_{TOL}(\theta_s,\theta_v,\phi) = T^{\downarrow}(\theta_s)T^{\uparrow}(\theta_v)\frac{1}{1-S\overline{\overline{\rho_s}}}\rho_s(\theta_s,\theta_v,\phi) + \rho_{aer}(\theta_s,\theta_v,\phi). \quad (1)$$

The reflectance ρ_{aer} is the aerosol contribution and ρ_s is the surface reflectance of the target, which is surrounded by a homogeneous environment of spectral reflectance $\overline{\overline{\rho_s}}$ that can be interpreted as the bihemispherical reflectance. The spherical albedo, S, of the aerosols describes the portion of upwelling radiance that is backscattered to the surface by the aerosol layer. The downward and upward transmittances throughout the aerosol layer are $T^{\downarrow}$ and $T^{\uparrow}$, respectively. The geometry of observation is defined by the zenith angles for illumination, θ_s, and viewing, θ_v, and the relative azimuth, ϕ, between the Sun and viewing directions. The variable τ stands for the aerosol optical thickness (AOT).

2.2. Model Parameterization

2.2.1. Surface Reflectance

[11] The land surface bidirectional reflectance distribution function (BRDF) is modeled by following a kernel-driven approach as in most satellite programs, either with variants [e.g., *Leroy et al.*, 1997; *Wanner et al.*, 1997; *Strahler et al.*, 1999; *Baret et al.*, 2007; *Muller et al.*, 2007] or integrally in the framework of the recent operational MSG program [*Geiger et al.*, 2008]. Such an approach means that the spectral land surface BRDF can be decomposed into a series of angular kernels representing elementary photometric processes (geometric, surface scattering effects) [*Roujean et al.*, 1992; *Wanner et al.*, 1995; *Lucht et al.*, 2000]. The original BRDF model of *Roujean et al.* [1992] is used here to simulate the surface reflectance ρ_S of equation (1). It reads:

$$\rho_s(\theta_s,\theta_v,\phi) = \sum_{i=0}^{2} k_i f_i(\theta_s,\theta_v,\phi) \quad (2)$$

$$f_0(\theta_s,\theta_v,\phi) = 1$$

$$f_1(\theta_s,\theta_v,\phi) = \frac{1}{2\pi}[(\pi-\phi)\cos\phi + \sin\phi]\tan\theta_s\tan\theta_v - \frac{1}{\pi}\left(\tan\theta_s + \tan\theta_v + \sqrt{\tan^2\theta_s + \tan^2\theta_v - 2\tan\theta_s\tan\theta_v\cos\phi}\right)$$

$$f_2(\theta_s,\theta_v,\phi) = \frac{4}{3\pi}\frac{1}{\mu_s+\mu_v}\left[\left(\frac{\pi}{2}-\xi\right)\cos\xi + \sin\xi\right] - \frac{1}{3}$$

where $\mu_s = \cos\theta_s$, $\mu_v = \cos\theta_v$, and ξ represents the phase angle for scattering defined as $\cos\xi = \cos\theta_s\cos\theta_v + \sin\theta_s\sin\theta_v\cos\phi$. The isotropic component has the unit kernel

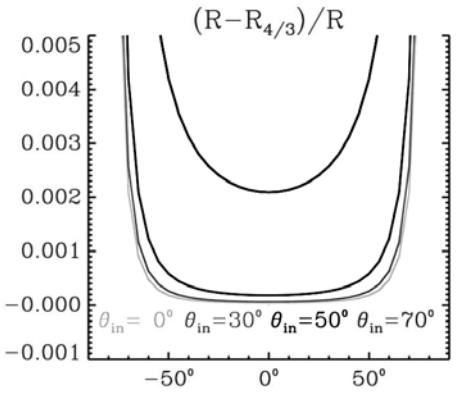

Figure 1. Comparison between the exact polynomial expansion $R(m\tau)$ and its approximate representation, $R_{4/3}$ $(m\tau)$, as a function of the incident angle (θ_{in}) and the outgoing angle (θ_{out}).

($f_0 = 1$). Surface kernels f_1 and f_2 represent the geometric and volume scattering kernels respectively. In practice, the k_i coefficients, which vary with wavelength, are retrieved from a best fit against a set of observations, as will be explained in section 2.3. The k_0 parameter stands for the isotropic component. Somewhat arbitrarily, k_0 matches a reflectance at nadir illumination and zenith view. The k_1 parameter is a geometric coefficient representing the optical roughness and k_2 is a coefficient for volumetric scattering.

2.2.2. Aerosol Reflectance

[12] The Mie theory explores the angular dependence of electromagnetic radiation scattering by small particles, typically submicrometer atmospheric aerosols. If the particles are assumed to resemble spheres, the corresponding phase function $P(\xi)$ is accurately approached by the Henyey-Greenstein (H-G) phase function $P_{H\text{-}G}$ [e.g., *Henyey and Greenstein*, 1941]. The H-G phase function has been widely considered in various applications [*Lumme and Bowell*, 1981; *Hartman and Domingue*, 1998], even sometimes in a two-term or three-term phase function [*Kattawar*, 1975; *Sturm*, 1981]. It reads:

$$P_{H-G}(\xi) = \frac{1-g^2}{(1+g^2-2g\cos(\pi-\xi))^{1.5}} \tag{3}$$

In equation (3), the asymmetry factor g varies from −1 (complete backscattering) to +1 (complete forward scattering), depending on the wavelength [*Fiebig et al.*, 2005]. The g parameter controls the size of the particle relative to the wavelength. Large particles show a pronounced forward scattering which is well reproduced by positive values of g. The attribution of a g value depends on the aerosol type. Clearly, this is a difficulty when different types of aerosol are mixed together. To represent dry continental nonabsorbing aerosols, *Fiebig et al.* [2005] have found values of g always slightly less than 0.5 over ARM (Atmospheric Radiation Measurements, http://www.arm.gov) stations. Note that absorbing aerosols have a larger asymmetry factor than nonabsorbing aerosols [*Trentmann et al.*, 2003]. Over Africa, a value of $g = 0.72$ is advised for Sahara dust [*Formenti et al.*, 2000] and a value of $g = 0.54$ has been reported for aerosols originating from biomass burning [*Ross et al.*, 1998]. In the remainder of the paper, we will privilege small size particles everywhere in taking $g = 0.6$, which corresponds to a continental aerosol, the most widespread aerosol category over land. The choice for such value will be evaluated in section 4.

[13] At the first scattering order, the approximated shape issued from the H-G aerosol scattering phase function is sufficient for practical integration in order to derive the first moment corresponding to the asymmetry factor, which governs the diffuse transmittance and reflectance factors [e.g., *Kokhanovsky et al.*, 2005]. Besides, the effects of multiple bouncing within the aerosol layer are to enhance the total aerosol reflectance ρ_{aer} and not to modify importantly the angular signature. Therefore, the multiple scattering component can be parameterized as a function of the AOT only, so as to obtain more efficient computation. A practical approximation for the reflectance of aerosols, ρ_{aer}, as a solution for radiation transfer within a turbid medium is devised as follows [e.g., *Hansen*, 1969; *Rozanov and Kokhanovsky*, 2006; *Seidel et al.*, 2008]:

$$\rho_{aer}(\theta_s,\theta_v,\phi;\tau) = \frac{\omega}{4}\frac{1}{\mu_s\mu_v}\frac{1}{m}P(\xi)R(m\tau)f_{ms}(\tau) \tag{4}$$

In equation (4), ω represents the aerosol single scattering albedo and $m = (\mu_s^{-1} + \mu_v^{-1})$ is the air mass factor. Note that nonabsorbing aerosol ($\omega = 1$) will be considered in the remainder of the paper. The correction factor $f_{ms}(\tau) = 1 + (7 - \tau)\tau/5$ and the light beam interception $R(m\tau) = [1 - e^{-m\tau}]$ give the attributes of the approximation. The latter is expressed as the ratio between two MacLaurin polynomial expansions $P_i(m\tau)$ and $Q_j(m\tau)$ where i and j indicate their respective degrees [*Padé*, 1899]. Based on numerical experiments, a very good equivalence is obtained with the following expression:

$$R_{4/3}(m\tau) = \frac{P_4(m\tau)}{Q_3(m\tau)} = \left[\frac{840 - 60m\tau + 20(m\tau)^2 - (m\tau)^3}{840 + 360m\tau + 60(m\tau)^2 + 4(m\tau)^3}\right].m\tau \tag{5}$$

In comparison with $R(m\tau)$, the approximation $R_{4/3}(m\tau)$ offers a relative precision of 0.3% for zenith angles up to 70° (Figure 1) and also a much better convergence of the solution than its Taylor series.

2.2.3. Aerosol Transmittance

[14] The aerosol transmission T and spherical albedo S follow an empirical parameterization devised by *Kokhanovsky et al.* [2005] in the case of using the H-G phase function:

$$T(\theta;\tau) = e^{-\tau/\mu} + \tau.e^{-u-v\tau-w\tau^2}, \tag{6}$$

$$S(\tau) = \tau\left(a.e^{-\tau/\alpha} + b.e^{-\tau/\beta} + c\right). \tag{7}$$

The parameters u, v, w depend on $\mu = \mu_{s,v}$ and are polynomial expressions of the asymmetry parameter g, which is also an input of the H-G phase function of equation (3). The constants a, b, c, α, β are parameterized using only polynomial expansion with respect to the asymmetry parameter.

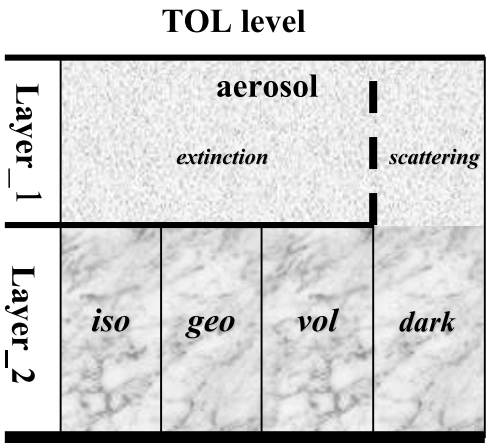

Figure 2. Sketch of the surface-aerosol associated medium under study.

The condition $\omega = 1$ allows holding tractable expressions [see *Kokhanovsky et al.*, 2005] and is consistent with the assumption for aerosol reflectance to consider a conservative medium.

2.2.4. Environmental Reflectance

[15] The homogeneous environmental reflectance of equation (1) is treated as the bihemispherical surface reflectance, which is the reflectance integrated over all suitable angular domains of both solar and viewing directions. Namely,

$$\overline{\overline{\rho_s}} = \frac{1}{\pi}\int_{2\pi}\left[\frac{1}{\pi}\int_{2\pi}\rho_s(\theta_s,\varphi_s,\theta_v,\varphi_v)\cos\theta_v d\Omega_v\right]\cos\theta_s d\Omega_s \qquad (8)$$

where $d\Omega_{s,v} = \sin\theta_{s,v}.d\theta_{s,v}.d\varphi_{s,v}$ is a solid angle and ρ_S is the surface reflectance as expressed in equation (2). Note that φ_S and φ_v are the azimuth angles for illumination and viewing, respectively.

2.2.5. Model Completion

[16] The reflectance ρ_{TOL} of equation (1) arising from a medium made up of an aerosol layer lying above a land surface layer is rewritten as a kernel-driven model. Gathering equation (1), (2), (3), (4), and (5) and segregating the variable τ, it follows that:

$$\rho_{TOL}(\theta_s,\theta_v,\phi) = \sum_{i=0}^{3} k_i f_i^{'}(\theta_s,\theta_v,\phi), \qquad (9)$$

where

$$f_{i=0,2}^{'}(\theta_s,\theta_v,\phi) = T^{\downarrow}(\theta_s)T^{\uparrow}(\theta_v)\frac{1}{1-S\overline{\overline{\rho_s}}}.f_{i=0,2}(\theta_s,\theta_v,\phi)$$

$$f_3^{'}(\theta_s,\theta_v,\phi) = \frac{\omega}{4}\frac{1}{\mu_s\mu_v}\frac{1-g^2}{(1+g^2+2g\cos\xi)^{1.5}} \cdot\left[\frac{840-60m\tau+20(m\tau)^2-(m\tau)^3}{840+360m\tau+60(m\tau)^2+4(m\tau)^3}\right][1+(7-\tau)\tau/5].$$

The coefficient k_3 identifies to τ, which variable also appears in the kernel functions. It will be formulated as an a priori value in the iterative procedure of the inversion scheme. Then, the value of τ is injected into the kernels until we obtain a convergent solution for τ. The surface BRDF parameters (k_0, k_1, k_2) on the previous day serve to calculate $\overline{\overline{\rho_s}}$ (equation (8)). The directional signatures of the modified volumetric and aerosol kernels, f'_2 and f'_3 respectively, both show an increase of the reflectance in the backward and forward directions, which may lead to an ill-posed problem. We will see later that an analysis of the differences in the characteristic timescales of these two signatures helps to circumvent the problem. The surface-aerosol system suggested in equation (9) is depicted in Figure 2. The innovative part relies on the assumption that there exists at least a portion of dark elements within the medium investigated.

2.3. Mathematical Design of the Retrieval Method

[17] In section 2.2, we designed a BRDF model for the aerosol-surface system, which can be computationally efficient. Our semiphysical approach aims to derive an algorithm that performs efficiently at a low computation cost and is particularly suitable for operational data processing. We start with a vector $Z = [\rho_{TOL}(\theta_s^1, \theta_v^1, \phi^1), \ldots, \rho_{TOL}(\theta_s^N, \theta_v^N, \phi^N)]$ representing a set of N observations at the TOL level. The kernel matrix $F = [f'_0 f'_1 f'_2 f'_3]$ includes the definition of the geometry of observations. A random noise υ with zero mean is considered, i.e.,

$$Z = FK + \upsilon. \qquad (10)$$

The solution to the inverse problem is obtained by adopting a recursive procedure [e.g., *Geiger et al.*, 2008]. In this respect, the vector of the parameters $K = [k_0\ k_1\ k_2\ k_3]$ and of the associated covariance matrix C_k read:

$$K = \frac{A^T B + C_{ap}^{-1}K_{ap} + C_{reg}^{-1}K_{reg}}{C_k^{-1}}, \qquad C_k = \frac{1}{A^T A + C_{ap}^{-1} + C_{reg}^{-1}} \qquad (11)$$

A is the "design matrix" with the elements $A_{ij} = F_{ij}/\sigma[\rho_{TOL}(\theta_s^j, \theta_v^j)]$, [e.g., *Press et al.*, 1992], where j is a given observation and i refers to the kernel number. The vector B represents the scaled reflectance with elements $B_j = \rho_{TOL}(\theta_s^j, \theta_v^j)/\sigma[\rho_{TOL}(\theta_s^j, \theta_v^j)]$. Greater importance is given to a reflectance measurement by means of a weighting factor of angular dependence, which is related to the inverse of the standard error estimates $\sigma[\rho_{TOL}(\theta_s^j, \theta_v^j)]$. The method assumes the existence of noncorrelated errors between the determination of the surface and the aerosol parameters, which are attributed to measurement noise and uncertainties in the atmospheric correction procedure (see Appendix A).

[18] The solution of equation (11) is obtained from a multiple linear regression. It can happen that the kernels are in a configuration of near colinearity and that retrieved values of the kernel coefficients may be uncertain. Hence, the matrix of covariance C_k cumulates the uncertainty $(A^T A)^{-1}$ on the retrieved k_i coefficients with the matrices K_{ap} and C_{ap} standing for a priori information. The matrices K_{reg} and C_{reg} use climatologic values to avoid numerical errors in computation. The latter are particularly meaningful in the resolution of ill-conditioned problems due to the use of

redundant or poor information. Various numerical experiments led to the following arbitrary choices: K_{reg} = [0, 0.03, 0.02, 0] and diagonal matrix C_{reg} = [10, 0.05, 0.5, 50] for the regularization terms. The quantity $\sqrt{C_k(3,3)}$ from the covariance matrix of equation (11) provides the uncertainty on k_3 (or τ), referred to below as $\Delta\tau$.

[19] The estimate of the state variable K at time step *J-1* is propagated in time using a linear state–transition model characterized by the prognostic model operator M, which fixes an a priori value for time step J:

$$K_{ap}^{J} = MK^{J-1}. \tag{12}$$

To initiate the regression, the value $K^{J-1} = K_{reg}$ is assigned at $J = 1$ in equation (11) and consequently equation (12) gives $K_{ap}^{J} = MK_{reg}$. Of course, the confidence on C_{reg} is very low at this stage of the process and K_{ap} has not impact on the estimation of K in case of cloud-free observations are available.

[20] The state vector covariance matrix C representing the uncertainty on K is also estimated:

$$C_{ap}^{J} = MC_k^{J-1}M^T + Q. \tag{13}$$

The matrix Q stands for the model noise variance and represents its uncertainty. Between two consecutive days, we assume that the surface properties are stationary. In consequence, the operator M is taken to be equal to the identity matrix. The variance matrix Q contains only terms on the diagonal because the a priori correlation errors between the coefficients k_i at *J-1* are currently set to zero in the algorithm. *Geiger et al.* [2008] advise the use of this simplification to avoid the lost of essential property of the covariance matrix C_{ap} of being positive defined related to numerical storage problem of a priori information. Nevertheless, this approximation does not substantially affect the uncertainty estimates. Thus, it can be written:

$$Q = \delta C_k^{J-1}. \tag{14}$$

The vector $\delta = [2^{2/t_0} - 1, 2^{2/t_1} - 1, 2^{2/t_2} - 1, 2^{2/t_3} - 1]$ depicts the characteristic temporal scales (t_0, t_1, t_2, t_3), expressed in day units, during which a physical process associated with a kernel could be realized. The isotropic parameter k_0 gives the spectral magnitude of the reflectance. Typically, at midlatitudes, it varies on a 5 day scale, i.e., $t_0 = 5$, corresponding to synoptic conditions, including rainfall and snow episodes. The geometric and volume scattering parameters, k_1 and k_2 respectively, contain the appropriate surface BRDF information. This latter varies more slowly in time in comparison with magnitude changes of the isotropic reflectance k_0, so a bimonthly period is deemed appropriate, i.e., $t_{1,2} = 60$. Finally, the aerosol component is expected to vary on very short time scale and therefore the aerosol parameter k_3 is not time constrained.

3. Evaluation of the Method

3.1. Implementation With SEVIRI Observations

[21] The present methodology for AOT retrieval is well designed for applications on a fine temporal scale. In this regard, and considering that aerosol variations operate on a short time scale, the implementation of the method in geostationary observation systems is meaningful. Historically, the instruments onboard geostationary platforms were equipped with a broad visible band having low sensitivity to aerosols. Since January 2004, the Spinning Enhanced Visible and Infra Red Imager (SEVIRI) sensor on the Meteosat Second Generation (MSG) satellite series is declared operational and performs quarter-hourly scans in the 650 nm visible band (560–710 nm), referred hereafter as VIS06. We consider calibrated and geolocated top-of-layer SEVIRI scenes of level 1.5. The observation geometry per SEVIRI pixel remains invariable but the illumination geometry between the sequenced scans changes during the day. Satellite and auxiliary input data required for aerosol retrieval are those of the Land SAF algorithms for BRDF and albedo retrievals [*Geiger et al.*, 2008]. Data preprocessing includes a thorough cloud screening and the resulting pixels are flagged noncloudy. Because the SEVIRI VIS06 is defined outside the spectrum of gaseous absorption, this later has a low influence. In fact, the Land SAF ground segment routinely removes the Rayleigh scattering and corrects for water vapor and ozone column absorption by using the Simplified Method for Atmospheric Correction (SMAC) [*Rahman and Dedieu*, 1994], which is a linear development of the 6S code (Second Simulation of the Satellite Signal in the Solar Spectrum) [*Vermote et al.*, 1997]. Water vapor content and atmospheric pressure are taken from output analysis of the European Centre for Medium-Range Weather Forecast (ECMWF) and the ozone content originates from the Total Ozone Mapping Spectrometer (TOMS) climatology. Each day, the set of SEVIRI reflectance values decontaminated with respect to atmospheric effects form the Z observing vector of equation (10). We associate the corresponding set of observation geometry with this vector through the vector F. The values of the kernel matrix K are obtained via equation (11), which provides simultaneous estimates of the daily SEVIRI AOT and surface BRDF. The latter also serves to calculate the surface albedo by angular and spectral integrations of the surface BRDF model of equation (2).

3.2. Synthetic Data Sets From the 6S Radiative Transfer Code

[22] The first step of the evaluation procedure of the method concerns the application to synthetic data sets. The 6S atmospheric radiative transfer model can simulate the radiance and reflectance of a cloudless atmosphere in the solar spectral region considering the atmospheric scattering and absorbing effects due to gases (water vapor, ozone, carbon dioxide, oxygen) and aerosols, and also the surface effects, including non-Lambertian surfaces. As for aerosols, 6S presents a wide range of possibilities, either by selecting one of the existing classes (continental, maritime, urban) or by using available optical properties (desert, stratospheric and biomass burning classes), or by computing the optical scattering parameters using Mie theory.

[23] The main inputs to 6S are the geometry of observation, the definition of a spectral range, the atmospheric model type for gaseous components, the aerosol model, and the ground reflectance. For the sake of coherence with the working assumptions of section 2.2, ozone and water vapor contents are fixed herein to a zero value, and a continental

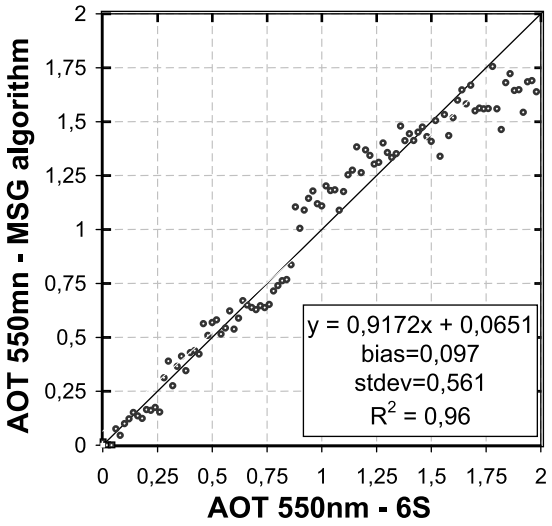

Figure 3. Comparison of the AOT at 550 nm between the operational method and 6S numerical experiments.

aerosol type is considered beforehand in 6S. In this case, we have $\omega = 0.88$ and the phase function is Mie theory for small particles with a forward peak and a mild backscattered effect. We consider the watershed of Blida (N 36° 30′, E 2° 53′, 230 m ASL), located in the north of Algeria, as viewed by SEVIRI on 1 July 2007 ($\theta_v = 40°$, $\phi_v = -175°$). The surface reflectance of the target, assumed to be Lambertian, is about 0.06 in the VIS06 band of SEVIRI. Variations of the AOT at 550 nm are within the range [0, 2.] with an increment of 0.05. For each value of AOT, we consider 17 values of the solar zenith angle from −80° to +80° with an angular step of 10°. We reproduce the diurnal cycle of the reflectance observed at the bottom at the surface level for an invariant aerosol quantity.

[24] The atmospheric 6S code determines the irradiance at ground level, the radiance at satellite level, and the distribution of radiance within the atmosphere in this optional wavelength range. More realistic situations are obtained by adding random noise and considering the noncorrelated errors expressed in Appendix A. A random ratio of the standard error of equation (A4) between −1 and 1 is added to the 6S reflectance value. As a result, it represents on average 17% of the perturbation in relative units between the 6S reflectance and the reflectance with random noise. Note that the synthetic data having the least influence, due to large associated angles, are also the most perturbed due to great uncertainty. For the sake of harmonization with the recursive method, we proceed as follows. The initial AOT is injected after a 5 day period of an aerosol-free atmosphere. From this period, the method provides a daily estimate of AOT at 550 nm to be compared with the initial AOT used to calculate the synthetic reflectance. Results of the comparison are reported in Figure 3, which reveals a fairly good statistical agreement since no bias is observed and relative error is low whatever the AOT value. The use of a priori information and the accumulation of observations during the day are intended to reduce the effects of the outliers coming, for instance, from residual cloud contamination since 17% of noise has a poor impact on the quality of the results.

3.3. Comparison With AERONET Data Sets

[25] To obtain some indication about the quantitative performance of the proposed algorithm, daily SEVIRI AOT values will now be considered with respect to those inverted from the global aerosol-monitoring Aerosol Robotic Network (AERONET, http://aeronet.gsfc.nasa.gov), which encompasses ground-based Sun photometer measurements. We use the AERONET Level 1.5 representing cloud-cleared data without final calibration [*Smirnov et al.*, 2000]. The aerosol properties are assumed invariable inside a SEVIRI pixel.

3.3.1. Midlatitude AERONET Stations

[26] We selected nine midlatitude stations located in contrasting climatic environments (Figure 4): Belsk (Poland), Blida (Algeria), Ispra, Rome, Venice (Italy), Carpentras, Villefranche (France), Evora (Portugal), and Kishinev (Moldova). Three of them are in coastal regions (Rome, Venice and Villefranche), one is at the edge of the desert (Blida), and several belong to downtown areas. Time series of daily SEVIRI pixel-based AOT at 650 nm are shown for the AERONET stations of Blida (Algeria), Carpentras (France), Kishinev (Moldova) and Rome (Italy) over the period from June 1st to September 30th, 2007 (Figure 5). We obtained conspicuous agreement between SEVIRI AOT and the AERONET AOT extrapolated at 650 nm using Ångström coefficient and Sun photometer data at 675 nm. The comparison in Figure 5 reveals generally good correlations. It is worth mentioning that the SEVIRI AOT values with relative uncertainty estimates larger than 75%, i.e., $\Delta\tau > 0.75\ \tau$, were discarded from this analysis. The lack of concomitant observations between AERONET and SEVIRI is also indicated on the graphs of Figure 5.

[27] For all stations, SEVIRI and AERONET indicate compliant trends for AOT values (Figure 5). Over Blida, several strong aerosol episodes are observed with AOT values beyond 0.5. Such events are generally well reproduced both in timing and intensity by the satellite-based method and are likely due to dust occurrence. On the other hand, the

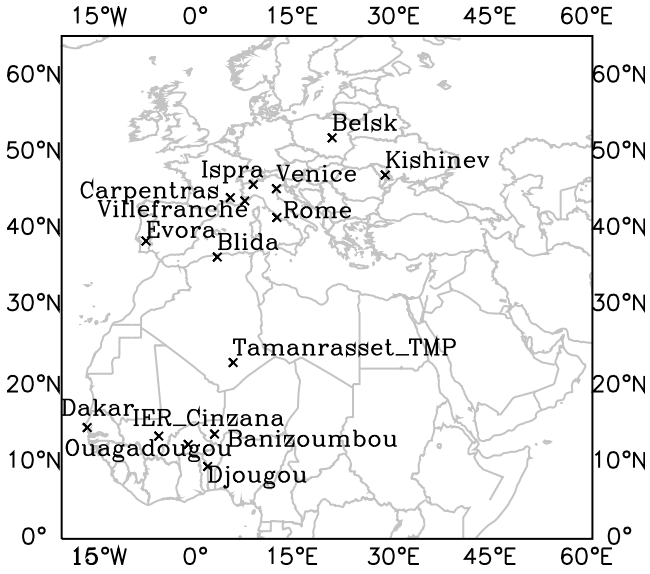

Figure 4. Location of the AERONET stations investigated in the present study.

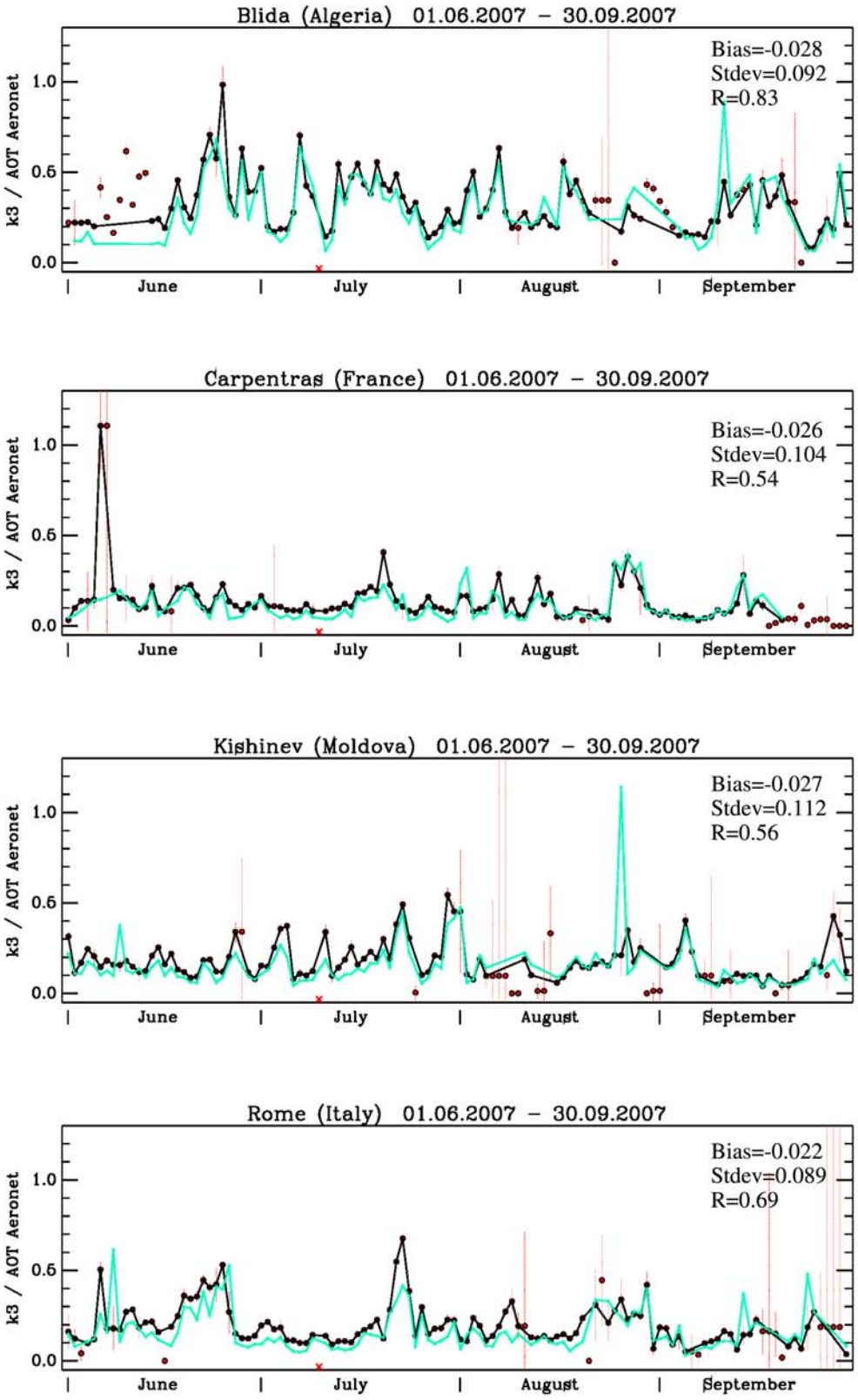

Figure 5. Time series of AOT values from SEVIRI (black) and AERONET (green) for four stations during the period 1 June 2007 to 30 September 2007. Data points are connected provided the AERONET level 1.5 AOT is available and the corresponding SEVIRI estimate is better than 75% of its value. The vertical red bars represent the uncertainty. A red cross on the *x* axis means no product available.

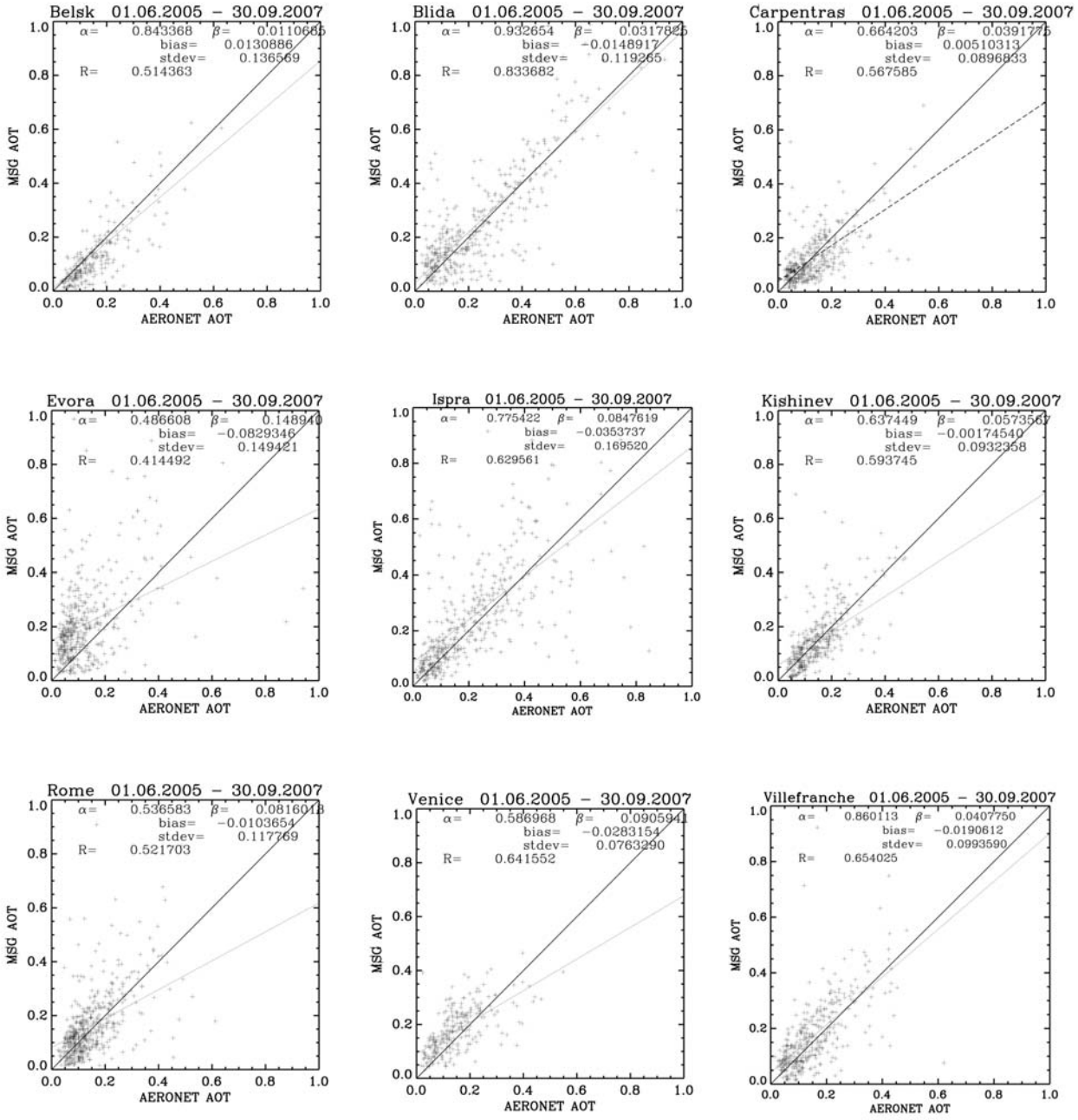

Figure 6. Scatterplots between AERONET and MSG AOT estimates between 1 June 2005 and 30 September 2007 for nine midlatitude stations: Belsk (Poland), Blida (Algeria), Villefranche (France), Carpentras (France), Evora (Portugal), Ispra (Italy), Kishinev (Moldova), Rome (Italy), and Venice (Italy).

medium-sized urban agglomeration of Carpentras shows lower AOT values and less variability. In Kishinev, the SEVIRI and AERONET AOT values are well correlated despite a SEVIRI pixel close to 10 km. This could be interpreted as a relatively slow evolution of the aerosol in the region. In Rome, the situation is complex because of the cumulative influence of maritime, desert and urban aerosols [*Gariazzo et al.*, 2007]. Some discrepancies are however noticeable. On August 24th in Kishinev, the dust event announced by AERONET is flagged as cloudy with SEVIRI. For reverse reason, SEVIRI indicated an aerosol peak in early June for Carpentras that is not reported on AERONET. A thorough examination reveals that it was initially present in AERONET Level 1, and then discarded in Level 1.5 after cloud screening. This means, first, that satellite and in situ data must be cross validated and, second, that the quality control is mainly based on our a priori knowledge. In this regard, aerosol events are typical of scenarios that cannot be anticipated.

[28] Figure 6 shows scatterplots of AOT estimates from SEVIRI versus AERONET for the nine sites and for the period between 1 June 2005 and 30 September 2007.

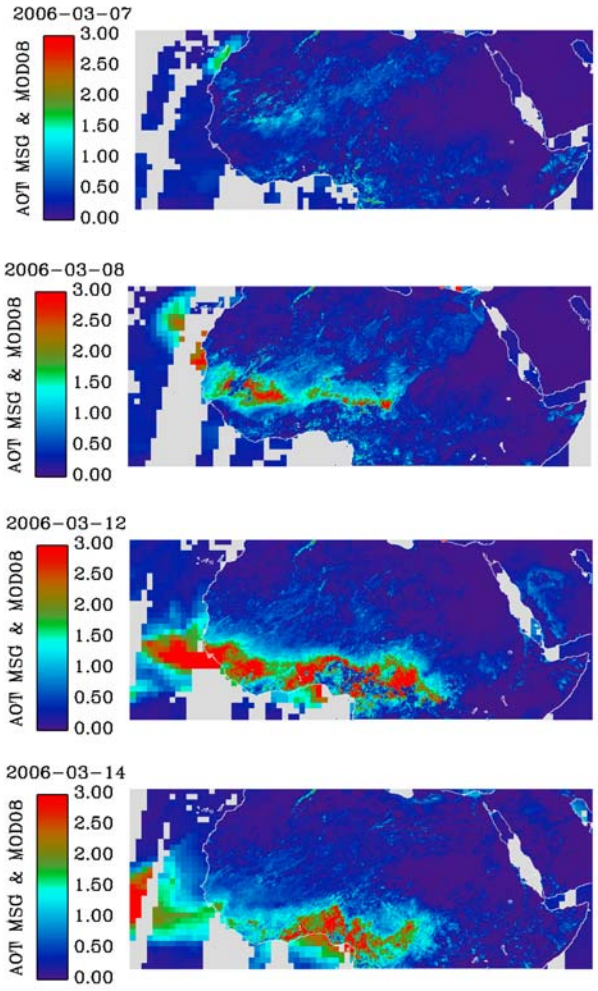

Figure 7. SEVIRI images of AOT at 650 nm on 7, 8, 12, and 14 March 2006. MODIS AOT at 550 nm from Collection 5 is superimposed over ocean. The geographic projection is 0.1° × 0.1° (over land for SEVIRI) and 1° × 1° (over ocean for MODIS).

Averaged daily AOT are close to 0.2 and, for any site, AOT values beyond 0.5 do not exceed a 10 day period. Main statistics (bias, standard deviation) change slightly with the site but still remain comparable. For the majority of the sites, the absolute value of the bias is below 0.05 and the standard deviation in absolute units is less than 0.15. Values of the correlation coefficient, R, depend on the site and are given between 0.41 and 0.83. In wintertime, the frequency of cloud cover combined with the grazing illumination degrades the quality of the estimations. For instance, from June to September, averaged statistics improve slightly toward an absolute bias of −0.015 (indicating a 49% reduction), a standard deviation of 0.122 (so reduced by 12%), and a correlation of 0.59 (improved by 4%).

3.3.2. West African AERONET Stations

[29] African dust originates from the Sahara and Sahel and is transported over large regions of the Earth. Because dust plumes are usually extensive and dynamically active, the monitoring of such aerosol events is better achieved via remote sensing data. Tracking aerosols is paramount in the framework of the African Monsoon Multidisciplinary Analysis (AMMA) program [*Redelsperger et al.*, 2006]. Particularly relevant is the period from March to August 2006 in the Western region of Africa. Figure 7 depicts the chronology of well-pronounced aerosol episode stretching over several days in early March 2006. On 7 March 2006, no aerosol concentration was yet noticeable. On 8 March 2006, an aerosol burden appeared suddenly along the intertropical front, probably from a source in the Bodele depression (lake Chad). During the following days, a pervasive aerosol plume stretched along the coastline of the Gulf of Guinea and intensified. Also observed were narrow thin dust plumes near the border between Mauritania and Senegal. Values of AOT up to 3 were not unusual. The phenomenon vanished totally on 25 March. The event is poorly evidenced with MODIS due to the difficulty of observing it over bright desert surfaces [*Kaufman et al.*, 1997]. It is worth emphasizing that we processed the SEVIRI pixels independently. Hence, the spatial coherence of the results reinforces the reliability of our method. Figure 8 illustrates the consistency between SEVIRI and AERONET AOT values for this event during the aerosol episode covered by six West African sites (Figure 4): Tamanrasset (Algeria), Dakar (Senegal), Cinzana (Mali), Banizoumbou (Niger), Ouagadougou (Burkina Faso), and Djougou (Benin). The analysis of the consistency of time series is in favor of a consolidation of the quality of the SEVIRI AOT estimate as the aerosol-laden situations are generally close to the corresponding AERONET AOT. In addition, the ground measurements also confirm the sudden character of the event occurring around 8 March 2006. In Figure 9, time series of AERONET and SEVIRI AOT values at four West African sites are plotted for the period from 1 March 2006 to 31 August 2006. Generally good correlations are observed between the two AOT products. Statistics for these North African sites are calculated including data from 1 March 2006 to 31 August 2006. Scatterplots are displayed in Figure 10 with the addition of 2 sites. On average, the absolute values are 0.014 for the bias, 0.294 for the standard deviation, with a correlation coefficient equals to 0.80. Hence, the statistical results show a slightly lower quality compared to the results obtained for Europe as previously discussed.

3.4. Validation With the Aerosol Radiative Forcing

[30] Climate forcing by aerosols is now the focus of a satellite strategy [*Anderson et al.*, 2003]. An indirect radiative effect is triggered by the aerosol's ability to affect cloud formation and radiative properties [*Ramanathan et al.*, 2001]. Direct radiative effects produced on the climate system by the aerosol scattering and absorption of solar radiation can vary extensively in both space and time. A recent study based on simulations showed that probability density functions obtained for the direct radiative forcing at the top of the atmosphere give a clear-sky, global, annual average of −1.9 W m^{-2} with standard deviation 0.3 W m^{-2} [*Bellouin et al.*, 2005]. Because of the large space and time variability of the aerosol load and type, uncertainty remains high in the particular context of extended temporal and spatial event studies. Mineral aerosols (dust), in particular, have a short lifetime and a large uncertainty remains with

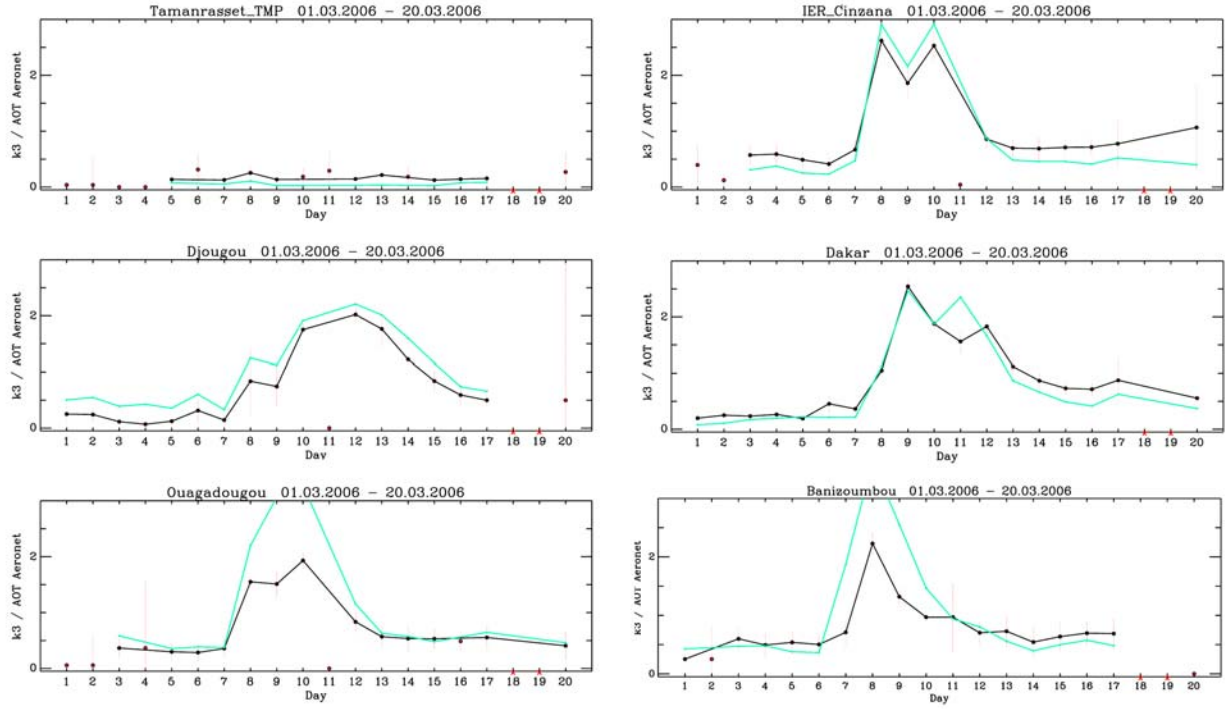

Figure 8. Time series of AERONET (green) and SEVIRI (black) AOT estimates during the period 1 to 20 March 2006, for six West African sites: Tamanrasset TMP (Algeria), Dakar (Senegal), IER Cinzana (Mali), Banizoumbou (Niger), Ouagadougou (Burkina Faso), and Djougou (Benin).

respect to their role in direct climate forcing [*Myhre and Stordal*, 2001].

[31] We assess here the aerosol radiative forcing in order to better support the reliability of the method by satisfying the criterion of energy conservation with respect to the surface-aerosol system. Results from our method are compared with computations from AERONET retrievals. We selected the AERONET stations of Blida (Algeria), Carpentras (France), Rome (Italy), and Tamanrasset (Algeria). Note that the Blida spot is a watershed located a few kilometers southwards of the AERONET station. We performed 6S simulations of the aerosol radiative forcing, using the TOL reflectance of the nearest cloud-free SEVIRI pixel and the correspondent geometry of observation as the main input. We restricted the simulations to solar zenith angles of less than 65° in order to minimize the influence of sky illumination. A continental-like aerosol class is prevalent in Europe and a desert-like class is highly probable over North Africa, which forced our options. The SEVIRI VIS06 band was introduced into 6S and AOT values at 550 nm were analyzed as a function of the aerosol type. The 6S numerical experiments were carried out with two independent forcing scenarios: (1) the SEVIRI VIS06 surface reflectance and (2) the AERONET AOT. The analysis covers the extended periods of spring 2006 and summer 2007, respectively for Tamanrasset and the 3 other sites. Look-Up Tables (LUTs) were built from 6S simulations of the SEVIRI reflectance in a nonabsorbing gas atmosphere and varying AOT at 550 nm with a step of 0.05 up to an AOT of 5. In scenario 1, the best fitted value was sought between SEVIRI and 6S reflectance values of an area bounded by a Lambertian surface or the predefined BRDF of *Roujean et al.* [1992] as the result of the inversion procedure described in section 3.1. The equivalent SEVIRI surface reflectance $< \rho_s(\theta_s, \theta_v, \phi) >$ to be compared with 6S output is defined as:

$$\langle \rho_s(\theta_s,\theta_v,\phi)\rangle = \rho_s(\theta_s,\theta_v,\phi)(1-f_v)(1-f_s) + \overline{\rho_s}(\theta_s)f_s + \overline{\rho_s}(\theta_v)f_v + \overline{\overline{\rho_s}}f_v f_s \quad (15)$$

where $\rho_s(\theta_s, \theta_v, \phi)$ is the surface bidirectional reflectance of equation (2), $\overline{\rho_s}(\theta_v)$ represents the directional-hemispherical reflectance (DHR) at angle θ_v, $\overline{\rho_s}(\theta_s)$ represents the DHR at angle θ_s, and $\overline{\overline{\rho}}_s$ is the bihemispherical reflectance. The quantities f_v and f_s stand for the ratio of diffuse to total radiation in the upward and downward directions, respectively. Based on a series of 6S numerical experiments, the following approximation is proposed:

$$f_{s,v} = \frac{1-e^{-\tau}}{1-(1-\mu_{s,v})e^{-\tau}} \quad (16)$$

In order to enhance the coherence between results, we retain only cases for which the absolute difference between $\langle \rho_s(\theta_s, \theta_v, \phi)\rangle$ of equation (15) and the 6S surface reflectance is less than 0.005. Note that this arbitrarily defined threshold value is much less than the absolute error accuracy of 7% on the surface retrieved from 6S [see *Kotchenova and Vermote*, 2007]. Moreover, in order to reduce the effects of the angular sampling and to exhibit fair comparisons between the different locations, we only show results

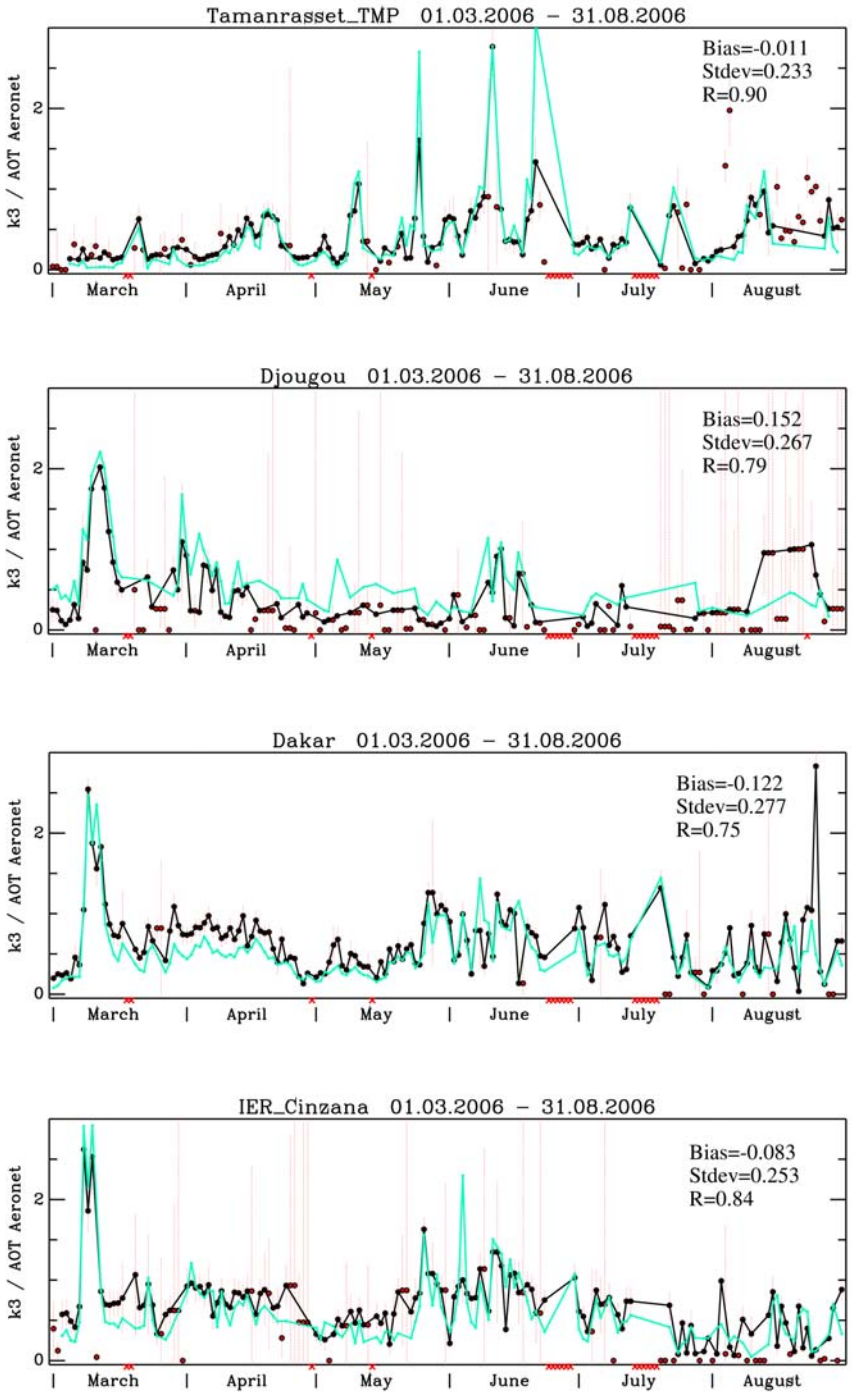

Figure 9. Same as Figure 5 but for four African sites and period from 1 March 2006 to 31 August 2006.

corresponding to scattering angles comprised between 35° and 135°. In Figure 11, we display times series of the retrieved 6S AOT for Blida over the extended summer period of 2007. Whenever available, the AERONET AOT at 550 nm is plotted. It is worth pointing out the better results obtained with the BRDF situation compared to the Lambertian, which highlights the importance of the surface anisotropy. Table 1 shows the statistical results between 6S and AERONET AOT values matching within a 1 h interval. It is noteworthy that the bias and the root mean square error (rmse) are generally low and that the satellite generally fails to report strong aerosol events, which explains the lower quality of the comparison during those periods. As for Carpentras, most aerosol episodes are well described and, in particular, the diurnal cycles on those days. The case of Rome is particularly complex because it is a mixture of different aerosol types (desert, urban, maritime aerosol). However, the chronology of surge in aerosol is well captured during the

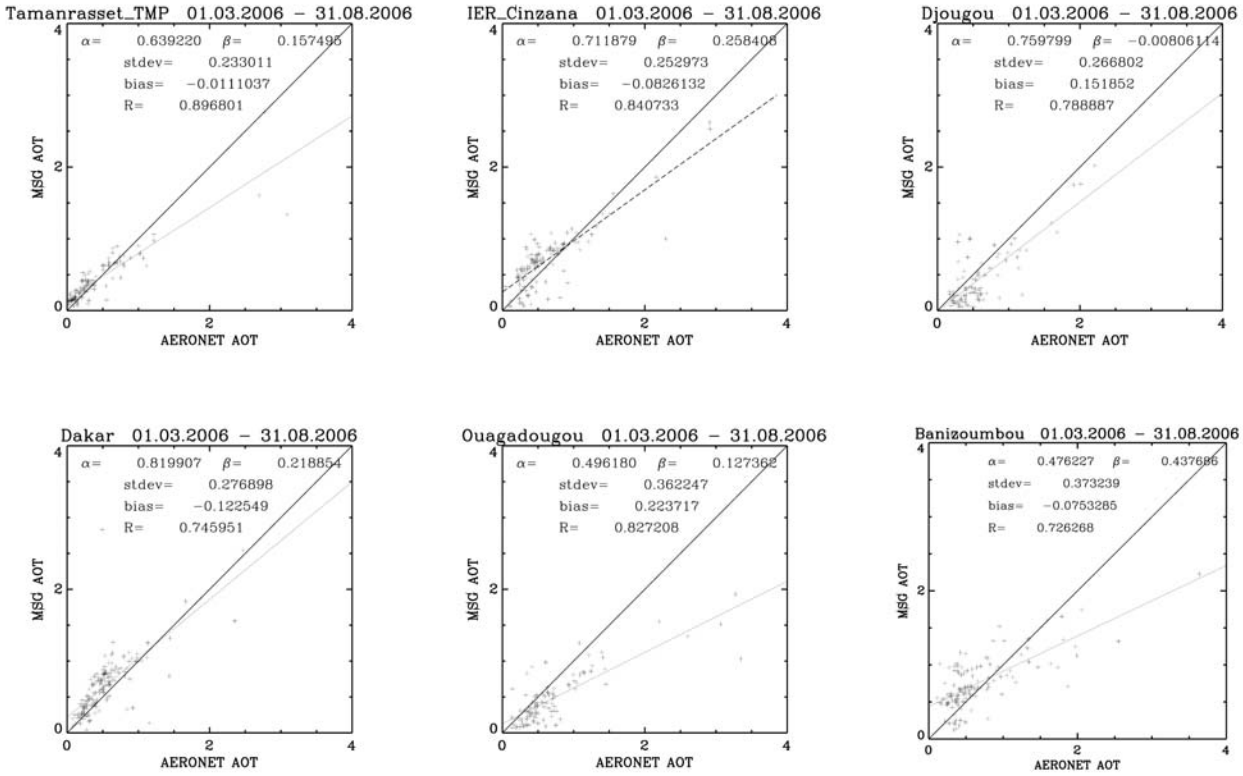

Figure 10. Scatterplots between AERONET and SEVIRI AOT estimates between 1 March 2005 and 31 August 2007 for six West African sites: Tamanrasset TMP (Algeria), Dakar (Senegal), IER Cinzana (Mali), Banizoumbou (Niger), Ouagadougou (Burkina Faso), and Djougou (Benin).

whole summer, as long AOT is less than 1. The site of Tamanrasset yields another case study because it is located in altitude and surrounded by desert essentially. Therefore, wind events may displace important aerosol load of dust resembling to large particles. It is notable that most aerosol episodes are well captured by the modeled AOT. On one hand, it seems difficult to reproduce AOT values typically beyond a value of 2. On the other hand, the retrieved AOT is somewhat underestimated even for observed AOT values less than 1. The situation may improve when increasing the value of the asymmetry factor as will be mentioned in section 4. Also, an analysis of the observations at mid-infrared wavelengths seems suitable for desert dust.

[32] The previous analysis served to isolate cases favorable for an evaluation of the aerosol radiative forcing. Assuming that AERONET AOT stands for truth, the difference between the atmospheric intrinsic radiance of the two scenarios indicates how the method satisfies the principle of the energy conservation although limited here to the visible spectrum. But major uncertainty on radiative budget occurs at shorter wavelength because of the larger impact of aerosols. The seasonally averaged values of the aerosol radiative forcing differences are less than 1 W/m^2 for all four stations (Figure 12). A negative difference indicates an overestimate of the atmospheric radiance from SEVIRI compared to AERONET. Notably, some values deviate from a few W/m^2 from the bias, in particular for European sites (Carpentras, Rome). The lack of spatial homogeneity there may explain such features resulting from a misrepresentation of AERONET data. The comparison with AERONET is particular commendable over North Africa. Interestingly, Blida and Tamanrasset show an overestimation of same magnitude despite they depict dark and bright targets, respectively. This outlines at least that an accurate retrieval of dust AOT seems to be relatively independent of the surface characteristics. The observed discrepancies between 6S and AERONET can be explained by the following given elements: (1) a misrepresentation of the in situ AOT measurement with respect to the pixel resolution of SEVIRI; (2) the mismatch of the AOT in cases of erratic variation as observed; (3) the ambiguity between aerosol load and thin clouds in respective data sets; (4) the choice of the aerosol type in 6S; and (5) the disregard of the diffuse illumination in the operational algorithm. Figure 12 reported to Figure 11 allows pointing out the discrepancies between satellite and in situ AOT values due to time shift.

3.5. Intercomparison With MODIS Aerosol

[33] In this section, we present the results of the comparison between SEVIRI and MODIS AOT values over Europe. *Kokhanovsky et al.* [2007] found large differences in instantaneous AOT retrievals obtained with different algorithms and instruments over land. These disagreements are explained by uncertainties in a priori assumptions made in the algorithms together with the differences in the various sensor characteristics and observation times. As for daily MODIS products in Collection 4, the aerosol retrieval over land adopted a 10 km segmentation corresponding to boxes

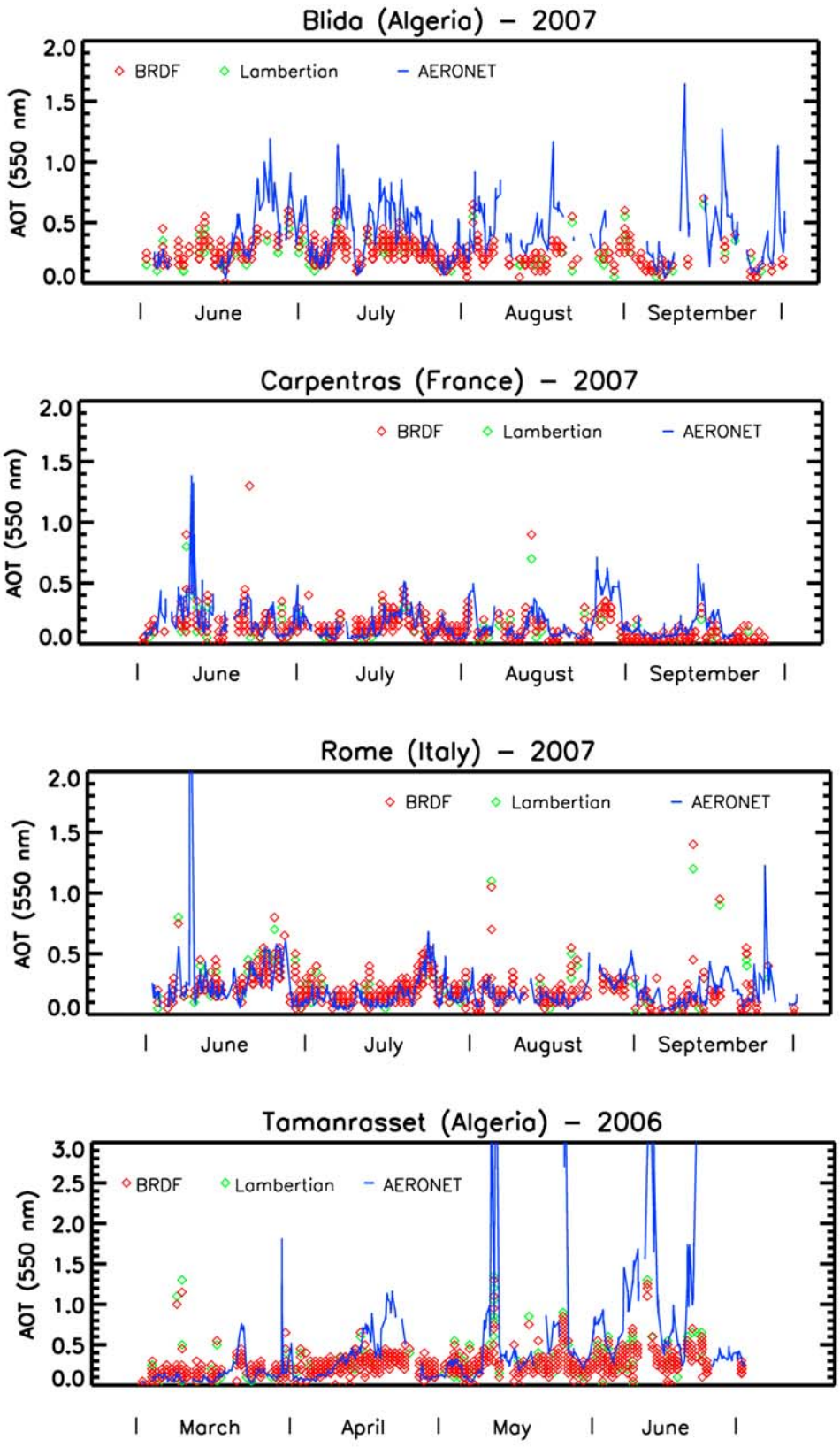

Figure 11. Time series of AOT at 550 nm retrieved from 6S code for the BRDF (red) and the Lambertian (green) cases. The corresponding AERONET AOT is plotted (solid blue lines). From top to bottom: Blida (Algeria), Carpentras (France), Rome (Italy), and Tamanrasset (Algeria).

Table 1. Statistical Results in Reflectance Absolute Unit Between Concomitant AOT Values Retrieved From 6S and From AERONET Measurements for the Four Selected Sites and Various Time Periods[a]

	⟨AOT⟩ 550 nm	RMSE Lambert	Bias Lambert	RMSE BRDF	Bias BRDF	N
			Blida (*Algeria*)			
2007						
June	0.354	0.042	0.122	0.038	0.085	37
July	0.357	0.017	0.125	0.016	0.100	127
August	0.270	0.046	0.050	0.052	0.032	15
September	0.180	0.028	0.041	0.029	0.026	17
			Carpentras (*France*)			
2007						
June	0.195	0.013	0.051	0.013	0.036	84
July	0.114	0.005	−0.006	0.005	−0.018	172
August	0.169	0.012	0.057	0.012	0.044	107
September	0.117	0.013	0.071	0.012	0.063	43
			Rome (*Italy*)			
2007						
June	0.235	0.007	0.005	0.008	−0.010	166
July	0.140	0.006	−0.036	0.006	−0.050	235
August	0.147	0.008	−0.023	0.009	−0.036	84
September	0.184	0.022	0.059	0.020	0.049	31
			Tamanrasset (*Algeria*)			
2006						
June	0.163	0.019	−0.008	0.020	−0.013	70
July	0.334	0.023	0.082	0.024	0.082	100
August	0.322	0.020	0.044	0.020	0.052	90
September	0.681	0.075	0.327	0.077	0.347	56

[a]Reflectance unit is [0,1]. The bias represents the distance of the 6S mean AOT from the mean AERONET AOT. RMSE is the root mean square error. N is the number of measurements used for the analysis.

of 400 pixels [*Remer et al.*, 2005]. In each box, the pixels exhibiting the 20% lowest and 50% highest reflectance factor values at 550 nm are discarded. Then, the regular retrieval path proposed by *Kaufman et al.* [1997] applies when at least 12 of the 400 pixels remain after the filtering process. MODIS Collection 5 is processed using a restructured method as discussed by *Levy et al.* [2007].

[34] Monthly MODIS Collection 5 products were confronted with similar SEVIRI AOT values on a 1° grid projection for the 2006 summer period over Europe. MODIS AOT values from Collection 5 at 550 nm were divided by the quantity $(\lambda_{550nm}/\lambda_{650nm})^{-\alpha}$ to be converted into the SEVIRI visible band at 650 nm. For this, we opted for an Ångström exponent $\alpha = 1.5$, which is a typical value observed for continental aerosols [e.g., *Elias et al.*, 2006]. This gave a conversion factor of 1.3. Here, we analyze only SEVIRI AOT estimates with high formal confidence, i.e., $\Delta\tau < 0.3\ \tau$. This corresponds to pixels with predominantly clear sky situations during the month-long period. In this way, the initial temporal definition of the respective products, daily with SEVIRI, instantaneous with MODIS, has less influence on the comparison procedure. The results show a rather scattered relationship (Figure 13) between the products as it could be expected [*Kokhanovsky et al.*, 2007].

[35] Figure 14 shows images of daily estimates for MODIS Collection 5 and SEVIRI AOT on three particular days (22 June 2005, 1 September 2005, and 8 September 2005) with mainly cloud free conditions. High AOT values are in general observed over the same region, which adds credit to the derivation of the two products. In addition, the two sensors concur in their reproduction of the dynamic patterns of AOT. Already, Figure 7 revealed the spatial continuity agreed to exist between SEVIRI AOT for land and the overlaid MODIS Collection 5 AOT for sea in the northwestern region of Africa. No multiplicative factor was applied to the MODIS AOT, as aerosols over ocean in that region are essentially dust particles having a zero Ångström exponent. The actual sources of discrepancies between the two AOT products are manifold. A quantitative evaluation of each of them will require further investigations. The underestimation of surface reflectance results in an overestimation of AOT and vice versa. Outliers such as introduced by undetected cloud or cloud shadowed pixels, inhomogeneous aerosol characteristics within the pixel, or deviations from the assumed standard atmosphere are additional sources of inaccuracy. Extremely low atmospheric aerosol concentrations might also hinder a successful approximation of aerosol type and AOT as outlined by *Dubovik and King* [2000].

3.6. Dependence of AOT on the Density of Urbanization

[36] In this section, we relate the SEVIRI AOT to the density of urbanization. First, we define a 'town density' factor within SEVIRI pixels by a reprojection of the GLC2000 land cover classification (IES Global Environment Monitoring Unit, Global land cover 2000 database, http://ies.jrc.ec.europa.eu/global-land-cover-2000) on the SEVIRI grid. Considering the histogram of classes over each MSG/SEVIRI pixel permits us to assign a degree of purity, or density, of the dominant class. The GLC2000 class 'Artificial surfaces and associated areas' is used here as an indicator of urbanization of an MSG/SEVIRI pixel, and the degree of purity of this class over this pixel characterizes the 'town

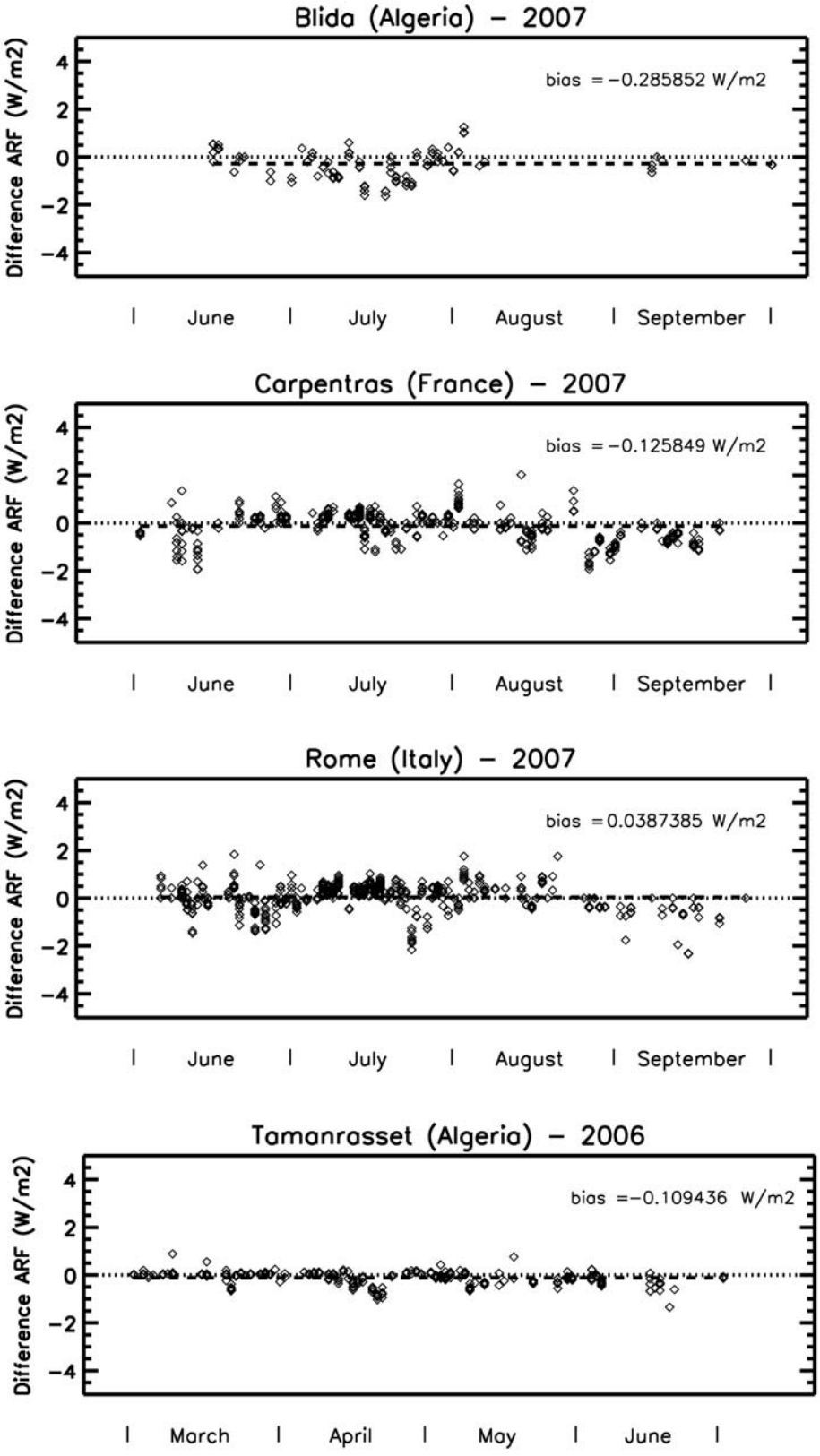

Figure 12. Time series of the difference in aerosol radiative forcing (ARF, in W/m^2) for visible spectrum between the case of BRDF surface reflectance forcing and AERONET forcing using 6S LUTs. From top to bottom: Blida (Algeria), Carpentras (France), Rome (Italy), and Tamanrasset (Algeria). Dashed line represents the seasonal bias (a positive value indicates an underestimate from the present method).

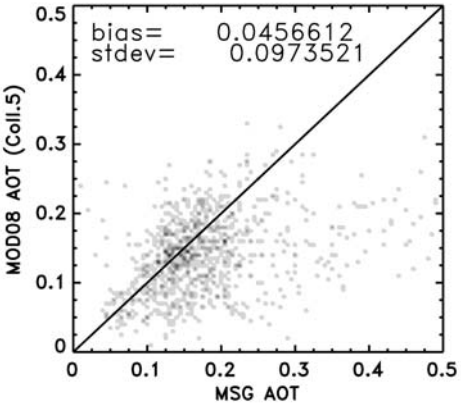

Figure 13. Scatterplot of SEVIRI and MODIS (Collection 5) monthly AOT values averaged over 1° × 1° boxes on the MSG disk from June 2006 to September 2006 at 0.65 μm. Only SEVIRI AOT retrievals with a high degree of confidence (see text) and the corresponding MODIS AOT are considered.

density.' Figure 15 shows mean SEVIRI AOT at 650 nm averaged over five full weeks in June 2006 according to the day of the week and the 'town density' in a region including Europe and North Africa (domain of Figure 14). The correspondence between the magnitude of the AOT and the relative proportion of a 'town density' is strong. Pixels having a 'town density' beyond 90% highlight the usual period of working days in relation to an increased traffic of motorized vehicles. This is consistent with previous urban aerosol reports [*Marr and Harley*, 2002a, 2002b; *Linacre and Geerts*, 2002; *Jin et al.*, 2005]. Results indicate an average exceeding 0.04 in AOT on working days (Figure 15). This is for instance compliant with a previous study conducted over the city of New York during the summer 2001 using AERONET data [*Jin et al.*, 2005].

4. Errors Analysis and Method Approximations

[37] This section is devoted to a quantitative analysis of the errors due to the necessary underlying physical approximations in order to develop and implement the method. Results also stress indirectly the potential limitations of application of our method. First of all, the coupling between molecular-aerosol scatterings can be a source of discrepancy for quantitative estimates of AOT [*Rozanov and Kokhanovsky*, 2005]. However, the phenomenon is almost negligible at increased wavelengths starting from the green spectrum. In the same way, the errors related to the vector character of light are non negligible at only wavelengths less than 650 nm in respect to specific geometric configurations of illumination and observation [*Rozanov and Kokhanovsky*, 2006].

[38] In the derivation of the reflectance model for aerosol, we took the option to better constrain the system in fixing, somewhat arbitrarily, some values for aerosols properties. This concerns the choice of the phase function, the value of the asymmetry factor, and to a lesser extent the magnitude of the single scattering albedo. There exists more scattering with small size particles, which are clearly the more representative over continent. Therefore, we privileged a value of the asymmetry factor corresponding to small size particles because the scattering processes are investigated. Figure 16 depicts the error on the phase function due to uncertainty on the asymmetric coefficient g for an uncertainty $\Delta g = 0.1$. If measurements close to the forward scattering peak are discarded, it appears that error on ΔP is 20% in average around the value $g = 0.6$.

[39] Because above analysis is performed using the H-G phase function, next step is to verify that this latter yields a good approximation of Mie theory. Figure 17 is intended to prove that the method is designed for small size particles through intercomparison with all aerosol types that could be observed over continent: black carbon (BC), desert dust (DU), organic matter (OM), sulphate (SU), and sea salt (SS). The construction of their respective phase function depends on several parameters [after *Toon and Ackerman*, 1981]: the coefficient of diffusion, the Mie parameter, the relative number of particles in the interval of size particles compared to total number in the distribution, the radius of the particles. Some aerosol types are particular sensitive to the particle size (DU, SS) while other (OM, SU) present characteristics depending on relative humidity, which means they can either be hydrophobic or hydrophilic. The results shown in Figure 17 reveal that the method has limitation for 2 cases: for dust and for urban areas. Note that it is not an issue for SS in the limit of small particles, which supports our choice. Figure 17 suggests the situation could improve for BC in taking $g = 0.3$ whereas it is not certain that decreasing the value of ω, because of enhanced absorption, would improve significantly the scores. With a disregard to BC, then a value of $g = 0.75$ would seem preferable in average, which is clearly more appropriate for DU and SS having their particle size larger than 0.5 μm (see Figure 17) although the use of a double H-G phase function should be advised. Consequently, error on ρ_{aer} would be more than 20% if these aerosol types were present. Nevertheless, the proposed method with actual set of parameters appears dependable for continental aerosol as far their composition is dominated by SU and OM, which is quite frequent. The method seems to be also efficient for SS having particle size smaller than 0.5 μm. Incidentally, the effects of relative humidity do not appear crucial apart very high values, which would concern rare situations. Another recommendation would be to restrict the inversion scheme to data sets comprised within an angular domain of scattering excluding the peaks, typically between 35° and 135° (see Figure 17).

[40] For global scale studies devoted to a retrieval of AOT, Figure 18 supports the options of the present work (see first paragraph of this section) because observations are in general no too strongly oriented in forward scattering direction during winter solstice, summer solstice and fall equinox. In this regard, our physical assumptions seem adapted to the angular capabilities that are offered by MSG/SEVIRI. Backscattered direction is prevalent in northeast Europe during boreal summer, in South Africa during boreal winter, and for most SEVIRI pixels over MSG disk during spring or fall equinoxes (Figure 18). But in Northern hemisphere, DU events occur preferably during boreal summer for which the SEVIRI sensor scans moderately in the backward scattering. It is remarkable that at the equinoxes, backscattering of the aerosols match with the hot spot

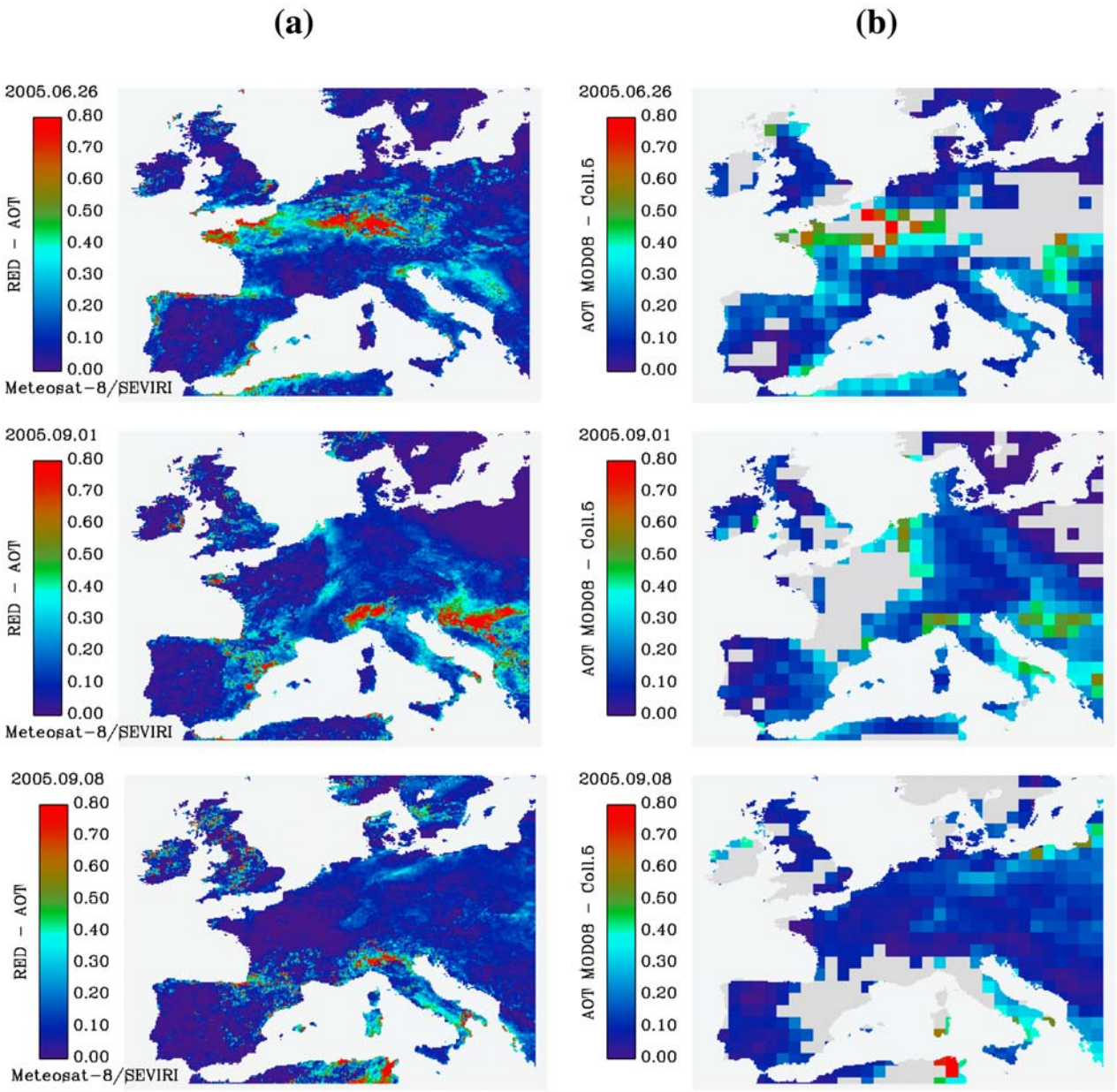

Figure 14. Images of daily AOT estimates at 0.65 μm for (top) 26 June 2005, (middle) 1 September 2005, and (bottom) 8 September 2005: (a) SEVIRI and (b) MODIS (Collection 5) on 1° × 1° boxes.

phenomenon, i.e., the reflectance peak in illumination direction, at local solar noon (Figure 18). Because the hot spot at surface level is difficult to sample with precision, DU particles of small size will be difficult to track at that times and hot spot observations should not be considered for further analysis.

[41] As far the aerosol type cannot be well determined, it is likely that Mie theory can be advantageously approached by H-G phase function. Besides, the approach is consistent with other reasonable assumptions on key parameters, g and ω mainly, provided they correspond to most representative situations over land surface. In this regard, opting for particles of small size with a mean relative humidity appears to be a sound trade-off. Further, the limited angular scanning of SEVIRI supports this choice because it is excluded measurements near the forward scattering peak.

5. Discussion and Conclusion

[42] An innovative method has been presented for obtaining routine estimates of the aerosol burden over land targets. The approach seems particularly well adapted to the high frequency of SEVIRI observations in order to retrieve a quality-controlled aerosol optical thickness. The multi-temporal approach takes advantage of a dynamic analysis of the directional properties of the aerosol and surface layers. The proposed algorithm operates a joint retrieval of aerosol and surface BRDF. A linear theory of the radiative transfer

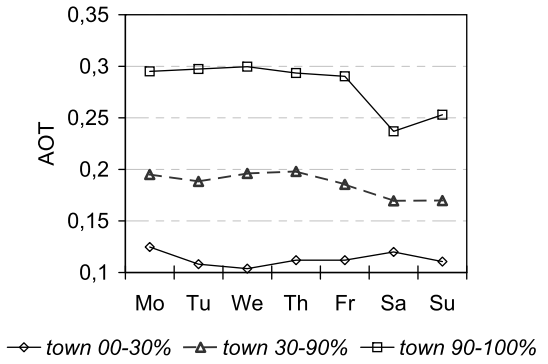

Figure 15. Aerosol optical thickness according to town density. Mean AOT from Monday, 29 May 2006, to Sunday, 2 July 2006 (5 complete weeks), versus day of the week and town density in a region including Europe and North Africa. Three categories were established using the GLC2000 land cover classification: MSG/SEVIRI pixels containing less than 30%, between 30% and 90%, and more than 90% of the class "artificial surfaces."

is suggested, and its inversion is based on a simplified Kalman filter. The method remains powerful to detect possible rapid changes of the surface layer because it analyzes the forward scattering signature of aerosols. The angular shape of BRDF is particularly sensitive to the presence of aerosols and allows aerosol and surface signals to be separated in all cases in assuming that at least an elementary dark target exists. The algorithm is computationally efficient for processing daily estimates over the full MSG disk, which ensures a geographic coverage of Europe, Africa and the eastern region of South America. It could be adapted for ocean at little expense in designing a BRDF adapted to sea surface.

[43] The SEVIRI space-time best coincident AOT values with ground-based AERONET indicate a high level of compliance for a given list of contrasted sites. In particular, the satisfactory agreement with AERONET AOT values supports the reliability of the method to reflect the short-time aerosol events appropriately. The method is also relevant for estimating dust events over bright surfaces where the presence of nonabsorbing aerosols diminishes the contrast that exists between the apparent and surface reflectance for heavy dust and no dust conditions. Further comparisons with instantaneous and monthly MODIS AOT values show the reliability of the quantitative estimates of the SEVIRI AOT although some mitigated conclusions have been pointed out. To increase the value of the method, we successfully evaluated its ability to report on the intensity of polluted areas on working days according to the density of urbanization.

[44] It is worth emphasizing the performance of the SEVIRI cloud mask since the case of an apparently hazy atmosphere, which could be due to very thin clouds, mostly appeared to be connected with strong aerosol events. Therefore, the error treatment could address special cases (broken cloud, cirrus), and thus contribute to the validity of the quality control of AERONET data for instance. Remaining cloud contamination would create a positive bias on the aerosol load measured by satellite. This undesirable effect can be substantially reduced in the case of geostationary observations compared to polar systems by a more severe selection considering the large number of slots.

[45] A challenging task is to promote the synergy of data from polar and geosynchronous platforms. It should be stressed that the method is not instrument-dependent but performs better with frequent observations. In this regard, spectral and angular information brought by polar system will be of added value for the retrieval of the aerosol spectral optical properties from SEVIRI. An autonomous determination of the aerosol class requires multiangular and wider spectral ranging sensors to be used in association. The foreseen merging of MSG and EPS (EUMETSAT Polar System) data in the framework of the Land SAF program is a very promising way to increase the grid resolution and extend the geographical coverage. Including data from different instruments does not require further methodological developments apart from technical aspects like the spectral normalization and the grid resampling, which yield an important asset of our method.

[46] Investigating the simultaneous retrieval of surface albedo and additional aerosol properties would certainly be a good direction for future research work to take. In this regard, an adaptation of the underlying physical assumptions to specific cases may improve the whole results, which seems mandatory in preparing hourly based AOT products. The impact of the additional aerosol kernel on the tunable parameters describing the surface properties, and hence also on surface albedo retrieval, has not yet been systematically studied. In the conventional three-kernel BRDF model approach, reflectance data perturbed by aerosol events can

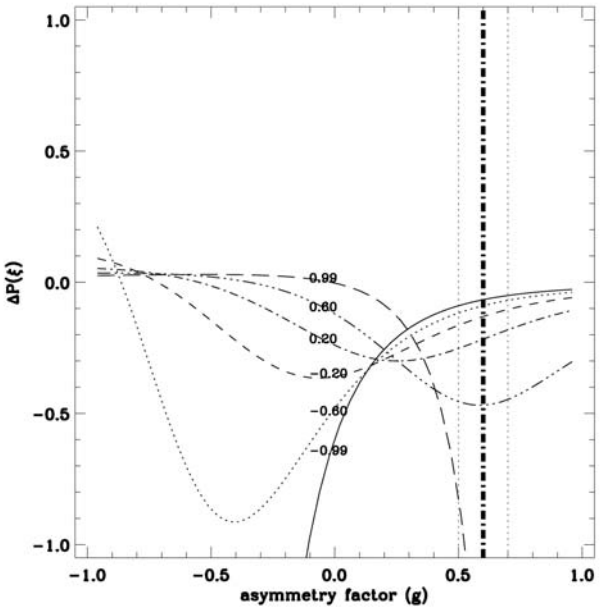

Figure 16. Absolute variations of the aerosol phase function $P(\xi)$ with the asymmetry parameter g for different values of the phase angle ξ in taking $\Delta g = 0.1$. Values of $\cos(\xi)$ are indicated on each curve. Dash-dotted vertical line delineates the value $g = 0.6$ taken as mean case. Dotted vertical lines represent the values $g = 0.5$ and $g = 0.7$.

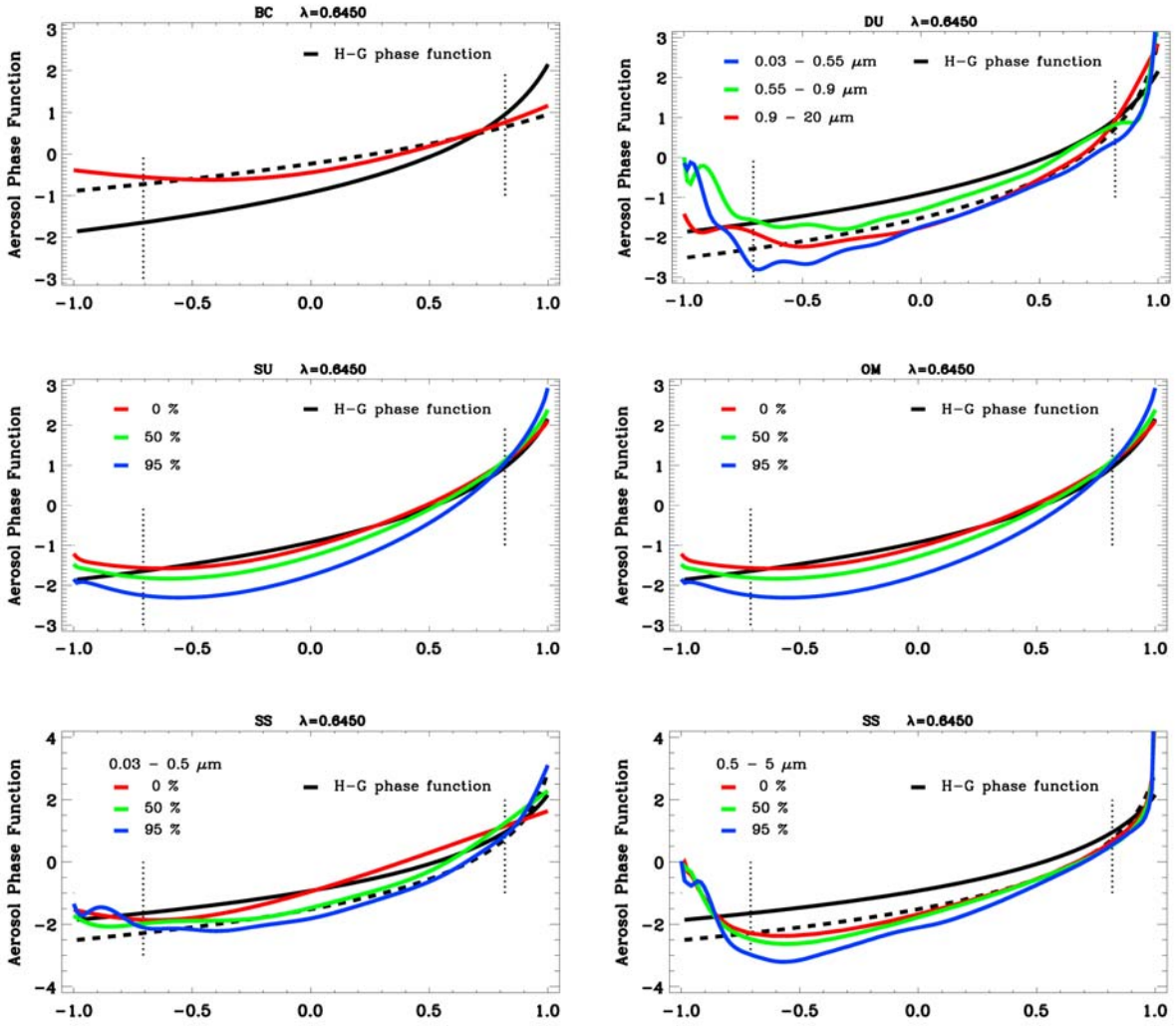

Figure 17. Henyey-Greenstein (H-G) phase function (black) for an asymmetry parameter $g = 0.6$ and Mie phase functions (color) as a function of the phase angle ξ (the supplementary angle of the scattering angle) for the wavelength 0.645 μm. Mie theory is shown for representative aerosol types: black carbon (BC), desert dust (DU), sulphate (SU), organic matter (OM), and sea salt (SS). Different colors of curve correspond to various intervals of particle sizes (in μm) or relative humidity (in percent). Dotted line delimits the angular domain [35°, 135°] of variations of the scattering angle ξ'. Dashed line represents values of H-G for $g = 0.3$ (BC) and $g = 0.75$ (DU, SS).

lead to spurious unphysical fluctuations of anisotropy parameters. Preliminary investigations of this issue tend to show that, in our approach, these residual fluctuations are well described by the aerosol kernel. This helps to improve the quality of the surface BRDF by reducing the initial spurious short-time variations in albedo time series. Moreover, the spatial resolution is not perceived as a strong constraint of our method given the fact that the spatial contrast is not exploited. Nonetheless, the selection for a large box, maybe on optimal device, increases the chance to observe a dark target over which the aerosol retrieval is more accurate. Our well-behaved algorithm will continue to undergo developments and refinements with intensive validation against ground measurements over longer periods, particularly for operational air quality forecasting. Considering the quantitative error estimate, the assimilation of SEVIRI AOT into numerical weather prediction models will offer new perspectives in term of aerosol radiative forcing and climate.

Appendix A: Estimation of Noncorrelated Errors

[47] To estimate $\sigma[\rho_{TOL}\ (\theta_s^j,\ \theta_v^j)]$ for the observation number j, we analyzed sets of SEVIRI observations over Europe having first a similar angular configuration. The period must be short enough to assume surface properties to be stationary, which is here from 2 to 4 June 2005 because of a low aerosol load according to MODIS. The estimate of

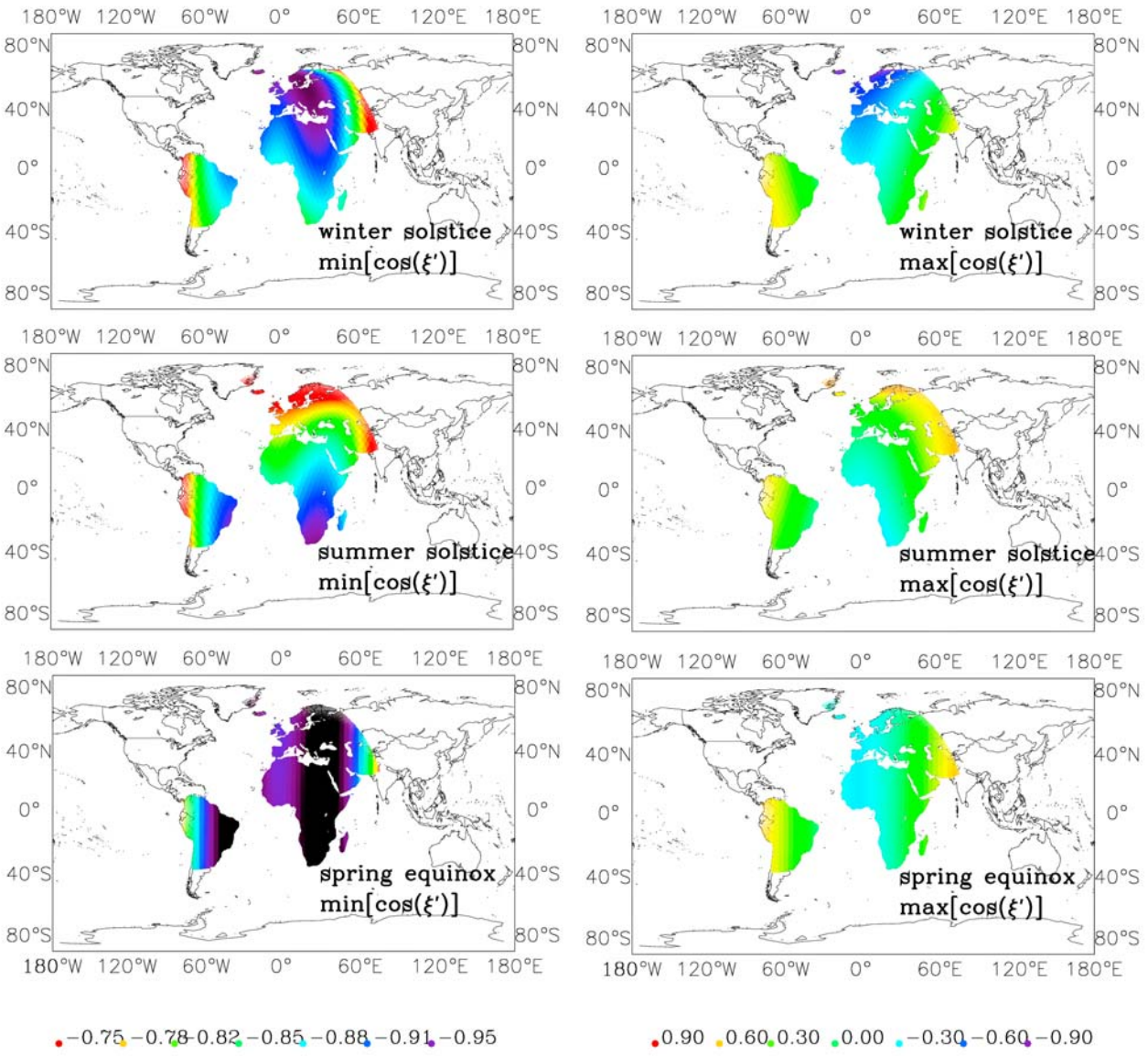

Figure 18. (right) Maximum and (left) minimum values of scattering angles obtained with SEVIRI over the MSG disk at (top) winter solstice, (middle) summer solstice, and (bottom) spring equinox. These maximum and minimum values are calculated to represent the 70% confidence interval of the SEVIRI scattering angle population.

noncorrelated errors is proposed here in the case of a geostationary system with SEVIRI. The directional dependence of $\sigma[\rho_{TOL}(\theta_s^j, \theta_v^j)]$ is a linear function of the relative air mass η:

$$\sigma\left[\rho_{TOL}\left(\theta_s^j, \theta_v^j\right)\right] = \sigma[\rho_{TOL}(\theta_s = 0, \theta_v = 0)]\eta. \quad \text{(A1)}$$

Within a good approximation, we obtain a Gaussian distribution of the reflectance difference $\Delta\rho_{TOL}$ for any pair of observations with corresponding azimuth variation, $\Delta\phi_s$, close to zero (see Figure A1). Given a value of the reflectance, we can express the root mean square error of $\Delta\rho_{TOL}$ for any pair of observations with corresponding azimuth variation, $\Delta\phi_s$ (see Figure A2) in the terms:

$$\sigma[\Delta\rho_{TOL}/\eta] := \sqrt{\left|\Delta(\rho_{TOL}/\eta)^2\right|}. \quad \text{(A2)}$$

Furthermore, the standard error between two variables having the same Gaussian error structure is $\sqrt{2}$ times as large. Normalizing by this quantity, we determine a standard error estimate for the reflectance factor, the limit of which is interpreted as:

$$\lim_{\Delta\phi_s \to 0} \sigma[\Delta\rho_{TOL}/\eta] = \sigma[\rho_{TOL}(\theta_s = 0, \theta_v = 0)]. \quad \text{(A3)}$$

As a result, it follows that the standard error $\sigma[\rho_{TOL}(\theta_s, \theta_v)]$ is a linear expression with $\rho_{TOL}(\theta_s, \theta_v)$. From equation (A1), it follows that:

$$\sigma\left[\rho_{TOL}\left(\theta_s^j, \theta_v^j\right)\right] = \left[c_1 + c_2\rho_{TOL}\left(\theta_s^j, \theta_v^j\right)\right]\eta. \quad \text{(A4)}$$

Best-estimate analysis gives $c_1 = 0.001$ and $c_2 = 0.07$.

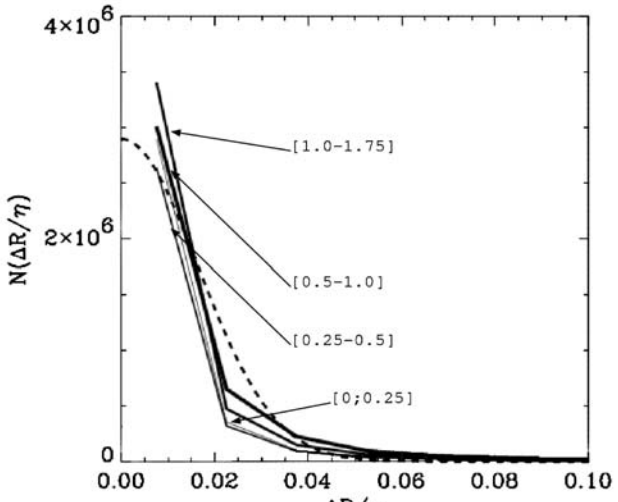

Figure A1. Probability density distribution of the quantity $\Delta\rho_{TOL}(\theta_s, \theta_v)/\eta$ (650 nm channel) for different values of $\Delta\phi_s$ on 2 June 2005 at 1200 UTC. From left to right on the plot, the solid curves correspond to $\Delta\phi_s$ intervals of [0.; 0.25] − [0.25; 0.5] − [0.5; 1] − [1; 1.75]. The total number of cases considered is close to 20 millions. The dashed line obeys a Gaussian law.

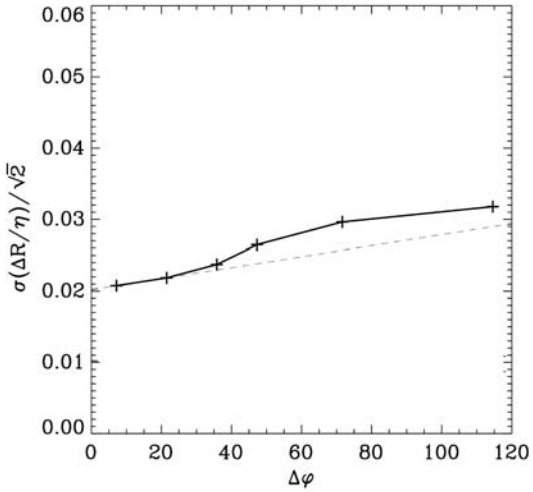

Figure A2. Standard deviation function of the normalized difference of reflectance versus angle of difference $\Delta\phi_s$ for SEVIRI at channel 650 nm and a reflectance value equal to 0.275.

[48] **Acknowledgments.** One of us (O.H.) received financial support from EUMETSAT (European Organization for the Exploitation of Meteorological Satellites) in the framework of the Satellite Application Facilities (SAF) program on Land Surface Analysis (LSA). We feel very indebted to the anonymous reviewers for their helpful suggestions and comments, which contributed to improving the understanding and readability of the manuscript. We would like also to thank Jean-Jacques Morcrette (European Centre for Medium-Range Weather Forecasts) for performing simulations from Mie theory and François-Marie Bréon (CEA/LSCE) for useful comments and suggestions.

References

Abdou, W. A., D. J. Diner, J. V. Martonchik, C. J. Bruegge, R. A. Kahn, B. J. Gaitley, K. A. Crean, L. A. Remer, and B. N. Holben (2005), Comparison of coincident Multiangle Imaging Spectroradiometer and Moderate Resolution Imaging Spectroradiometer aerosol optical depths over land and ocean scenes containing Aerosol Robotic Network sites, *J. Geophys. Res.*, *110*, D10S07, doi:10.1029/2004JD004693.

Anderson, T. L., R. J. Charlson, S. E. Schwartz, R. Knutti, O. Boucher, H. Rodhe, and J. Heintzenberg (2003), Climate forcing by aerosols—A hazy picture, *Science*, *300*, 1103–1104, doi:10.1126/science.1084777.

Baret, F., et al. (2007), LAI, fAPAR and fCover CYCLOPES global products derived from VEGETATION. Part 1: Principles of the algorithm, *Remote Sens. Environ.*, *110*, 275–286, doi:10.1016/j.rse.2007.02.018.

Bellouin, N., O. Boucher, J. Haywood, and M. S. Reddy (2005), Global estimate of aerosol direct radiative forcing from satellite measurements, *Nature*, *438*, 1138–1141, doi:10.1038/nature04348.

Boucher, O. (1998), On aerosol direct shortwave forcing and the Henyey-Greenstein phase function, *J. Atmos. Sci.*, *55*, 128–134, doi:10.1175/1520-0469(1998)055<0128:OADSFA>2.0.CO;2.

Dubovik, O., and M. D. King (2000), A flexible inversion algorithm for retrieval of aerosol optical properties from Sun and sky radiance measurements, *J. Geophys. Res.*, *105*(D16), 20,673–20,696, doi:10.1029/2000JD900282.

Elias, T., and J.-L. Roujean (2008), Estimation of the aerosol radiative forcing at ground level, over land, and in cloudless atmosphere, from METEOSAT-7 observation: Method and case study, *Atmos. Chem. Phys.*, *8*, 625–636.

Elias, T., A. M. Silva, N. Belo, S. Pereira, P. Formenti, G. Helas, and F. Wagner (2006), Aerosol extinction in a remote continental region of the Iberian Peninsula during summer, *J. Geophys. Res.*, *111*, D14204, doi:10.1029/2005JD006610.

Fiebig, M., C. Stein, F. Schröder, P. Feldpausch, and A. Petzold (2005), Inversion of data containing information on the aerosol particle size distribution using multiple instruments, *J. Aerosol Sci.*, *36*, 1353–1372, doi:10.1016/j.jaerosci.2005.01.004.

Formenti, P., M. O. Andreae, and J. Lelieveld (2000), Measurements of aerosol optical depth above 3570 m asl in the North Atlantic free troposphere: Results from ACE-2, *Tellus, Ser. B*, *52*, 678–693.

Gariazzo, C. C., et al. (2007), A gas/aerosol air pollutants study over the urban area of Rome using a comprehensive chemical transport model, *Atmos. Environ.*, *41*, 7286–7303, doi:10.1016/j.atmosenv.2007.05.018.

Geiger, B., D. Carrer, L. Franchistéguy, J. L. Roujean, and C. Meurey (2008), Land surface albedo derived on a daily basis from Meteosat Second Generation observations, *IEEE Trans. Geosci. Remote Sens.*, *46*, 3841–3856, doi:10.1109/TGRS.2008.2001798.

Hansen, J. E. (1969), Radiative transfer by doubling very thin layers, *Astrophys. J.*, *155*, 565–573, doi:10.1086/149892.

Hartman, B., and D. Domingue (1998), Scattering of light by individual particles and the implications for models of planetary surfaces, *Icarus*, *131*, 421–448, doi:10.1006/icar.1997.5861.

Haywood, J., and O. Boucher (2000), Estimates of the direct and indirect radiative forcing due to tropospheric aerosols: A review, *Rev. Geophys.*, *38*, 513–543, doi:10.1029/1999RG000078.

Haywood, J., P. Francis, S. Osborne, M. Glew, N. Loeb, E. Highwood, D. Tanré, G. Myhre, and P. Formenti (2003), Radiative properties and direct radiative effect of Saharan dust measured by the C-130 aircraft during SHADE: 1. Solar spectrum, *J. Geophys. Res.*, *108*(D18), 8577, doi:10.1029/2002JD002687.

Henyey, L. G., and J. L. Greenstein (1941), Diffuse radiation in the galaxy, *Astrophys. J.*, *93*, 70–83, doi:10.1086/144246.

Herman, M., J.-L. Deuzé, A. Marchand, B. Roger, and P. Lallart (2005), Aerosol remote sensing from POLDER/ADEOS over the ocean: Improved retrieval using a nonspherical particle model, *J. Geophys. Res.*, *110*, D10S02, doi:10.1029/2004JD004798.

Holben, B. N., et al. (1998), AERONET: A federated instrument network and data archive for aerosol characterization, *Remote Sens. Environ.*, *66*, 1–16, doi:10.1016/S0034-4257(98)00031-5.

Ichoku, C., L. A. Remer, and T. F. Eck (2005), Quantitative evaluation and intercomparison of morning and afternoon Moderate Resolution Imaging Spectroradiometer (MODIS) aerosol measurements from Terra and Aqua, *J. Geophys. Res.*, *110*, D10S03, doi:10.1029/2004JD004987.

Intergovernmental Panel on Climate Change (2007), *Climate Change 2007: The Physical Science Basis, Contribution of Working Group I to the Fourth Assessment Report of the Intergovernmental Panel on Climate Change S. Solomon*, edited by S. Solomon et al., Cambridge Univ. Press, New York.

Jeong, M.-J., and Z. Li (2005), Quality, compatibility, and synergy analyses of global aerosol products derived from the advanced very high resolution radiometer and Total Ozone Mapping Spectrometer, *J. Geophys. Res.*, *110*, D10S08, doi:10.1029/2004JD004647.

Jeong, M.-J., Z. Li, D. A. Chu, and S.-C. Tsay (2005), Quality and compatibility analyses of global aerosol products derived from the advanced very high resolution radiometer and Moderate Resolution Imaging Spectroradiometer, *J. Geophys. Res.*, *110*, D10S09, doi:10.1029/2004JD004648.

Jin, M., J. M. Shepherd, and M. D. King (2005), Urban aerosols and their variations with clouds and rainfall: A case study for New York and Houston, *J. Geophys. Res.*, *110*, D10S20, doi:10.1029/2004JD005081.

Kahn, R. A., B. J. Gaitley, J. V. Martonchik, D. J. Diner, K. A. Crean, and B. Holben (2005), Multiangle Imaging Spectroradiometer (MISR) global aerosol optical depth validation based on 2 years of coincident Aerosol Robotic Network (AERONET) observations, *J. Geophys. Res.*, *110*, D10S04, doi:10.1029/2004JD004706.

Kattawar, G. W. (1975), A three-parameter analytic phase function for multiple scattering calculations, *J. Quant. Spectrosc. Radiat. Transfer*, *15*, 839–849, doi:10.1016/0022-4073(75)90095-3.

Kaufman, Y. J., D. Tanré, L. A. Remer, E. F. Vermote, A. Chu, and B. N. Holben (1997), Operational remote sensing of tropospheric aerosol over land from EOS moderate resolution imaging spectroradiometer, *J. Geophys. Res.*, *102*(D14), 17,051–17,068, doi:10.1029/96JD03988.

Kaufman, Y. J., D. Tanré, and O. Boucher (2002), A satellite view of aerosols in the climate system, *Nature*, *419*, 215–223, doi:10.1038/nature01091.

Knapp, K. R., R. Frouin, S. Kondragunta, and A. Prados (2005), Toward aerosol optical depth retrievals over land from GOES visible radiances: Determining surface reflectance, *Int. J. Remote Sens.*, *26*(18), 4097–4116, doi:10.1080/01431160500099329.

Kokhanovsky, A. A., and G. de Leeuw (2009), *Satellite Aerosol Remote Sensing Over Land*, Springer, New York.

Kokhanovsky, A. A., and T. Y. Nakajima (1998), The dependence of phase functions of large transparent particles on their refractive index and shape, *J. Phys. D Appl. Phys.*, *31*, 1329–1335, doi:10.1088/0022-3727/31/11/006.

Kokhanovsky, A. A., B. Mayer, and V. V. Rozanov (2005), A parameterization of the diffuse transmittance and reflectance for aerosol remote sensing problems, *Atmos. Res.*, *73*, 37–43, doi:10.1016/j.atmosres.2004.07.004.

Kokhanovsky, A. A., et al. (2007), Aerosol remote sensing over land: A comparison of satellite retrievals using different algorithms and instruments, *Atmos. Res.*, *85*, 372–395, doi:10.1016/j.atmosres.2007.02.008.

Kotchenova, S. Y., and E. F. Vermote (2007), Validation of a vector version of the 6S radiative transfer code for atmospheric correction of satellite data. Part II. Homogeneous Lambertian and anisotropic surfaces, *Appl. Opt.*, *46*, 4455–4464, doi:10.1364/AO.46.004455.

Kusmierczyk-Michulec, J., and G. de Leeuw (2005), Aerosol optical thickness retrieval over land and water using Global Ozone Monitoring Experiment (GOME) data, *J. Geophys. Res.*, *110*, D10S05, doi:10.1029/2004JD004780.

Lenoble, J. (Ed.) (1985), *Radiative Transfer in Scattering and Absorbing Atmospheres*: Standard Computational Procedures, A. Deepak, Hampton, Va.

Leroy, M., J. L. Deuzé, F. M. Bréon, O. Hautecoeur, M. Herman, J. C. Buriez, D. Tanré, S. Bouffiès, P. Chazette, and J. L. Roujean (1997), Retrieval of atmospheric properties and surface bidirectional reflectances over the land from POLDER/ADEOS, *J. Geophys. Res.*, *102*(D14), 17,023–17,037, doi:10.1029/96JD02662.

Levy, R. C., L. A. Remer, S. Mattoo, E. F. Vermote, and Y. J. Kaufman (2007), Second-generation operational algorithm: Retrieval of aerosol properties over land from inversion of Moderate Resolution Imaging Spectroradiometer spectral reflectance, *J. Geophys. Res.*, *112*, D13211, doi:10.1029/2006JD007811.

Linacre, E., and B. Geerts (2002), Estimating the annual mean screen temperature empirically, *Theor. Appl. Climatol.*, *71*, 43–61, doi:10.1007/s704-002-8207-4.

Liou, K. N., and J. E. Hansen (1971), Intensity and polarization for single scattering by polydisperse spheres: A comparison of ray optics and Mie theory, *J. Atmos. Sci.*, *28*, 995–1004, doi:10.1175/1520-0469(1971)028<0995:IAPFSS>2.0.CO;2.

Lucht, W., C. B. Schaaf, and A. H. Strahler (2000), An algorithm for the retrieval of albedo from space using semiempirical models, *IEEE Trans. Geosci. Remote Sens.*, *38*, 977–998, doi:10.1109/36.841980.

Lumme, K., and E. Bowell (1981), Radiative transfer in the surfaces of atmosphereless bodies, I. Theory, *Astron. J.*, *86*, 1694–1704, doi:10.1086/113054.

Marr, L. C., and R. A. Harley (2002a), Modelling the effect of weekday-weekend differences in motor vehicle emissions on photochemical air pollution in central California, *Environ. Sci. Technol.*, *36*, 4099–4106, doi:10.1021/es020629x.

Marr, L. C., and R. A. Harley (2002b), Spectral analysis of weekday-weekend differences in ambient ozone, nitrogen oxide, and non-methane hydrocarbon time series in California, *Atmos. Environ.*, *36*, 2327–2335, doi:10.1016/S1352-2310(02)00188-7.

Mishchenko, M. I., L. D. Travis, and D. W. Mackowski (1996), T-matrix computations of light scattering by non-spherical particles: A review, *J. Quant. Spectrosc. Radiat. Transfer*, *55*, 535–575, doi:10.1016/0022-4073(96)00002-7.

Mishchenko, M., J. N. Dlugach, E. G. Yanovitskij, and N. T. Zakharova (1999), Bidirectional reflectance of flat, optically thick particulate layers: An efficient radiative transfer solution and applications to snow and soil surfaces, *J. Quant. Spectrosc. Radiat. Transf.*, *63*, 409–432, doi:10.1016/S0022-4073(99)00028-X.

Muller, J.-P., R. Preusker, J. Fischer, M. Zuhlke, C. Brockmann, and P. Regner (2007), ALBEDOMAP: MERIS land surface albedo retrieval using data fusion with MODIS BRDF and its validation using contemporaneous EO and in situ data products, in *2007 IEEE International Geoscience and Remote Sensing Symposium*, pp. 2404–2407, Inst. of Electr. and Electron. Eng., Piscataway, N. J.

Myhre, G., and F. Stordal (2001), Global sensitivity experiments of the radiative forcing due to mineral aerosols, *J. Geophys. Res.*, *106*(D16), 18,193–18,204, doi:10.1029/2000JD900536.

Padé, H. (1899), Mémoire sur les développements en fractions continues de la fonction exponentielle, in*Annales Scientifiques de l'École Normale Supérieure*, *Sér. 3*, vol. 16, pp.395–426, Gauthier-Villas, Paris.

Pinty, B., F. Roveda, M. M. Verstrate, N. Gobron, Y. Govaerts, J. V. Martonchik, D. J. Diner, and R. A. Kahn (2000), Surface albedo retrieval from Meteosat, *J. Geophys. Res.*, *105*(D14), 18,099–18,134, doi:10.1029/2000JD900113.

Popp, C., A. Hauser, N. Foppa, and S. Wunderle (2007), Remote sensing of aerosol optical depth over Central Europe from MSG-SEVIRI data and accuracy assessment with ground-based AERONET measurements, *J. Geophys. Res.*, *112*, D24S11, doi:10.1029/2007JD008423.

Press, W. H., S. A. Teukolsky, W. T. Vetterling, and B. P. Flannery (1992), *Numerical Recipes in Fortran*, Cambridge Univ., New York.

Rahman, H., and G. Dedieu (1994), SMAC: A simplified method for the atmospheric correction of satellite measurements in the solar spectrum, *Int. J. Remote Sens.*, *15*(1), 123–143, doi:10.1080/01431169408954055.

Ramanathan, V., P. J. Crutzen, J. T. Kiehl, and D. Rosenfeld (2001), Aerosols, climate, and the hydrological cycle, *Science*, *294*, 2119–2124, doi:10.1126/science.1064034.

Redelsperger, J. L., C. Thorncroft, A. Diedhiou, T. Lebel, D. J. Parker, and J. Polcher (2006), African Monsoon Multidisciplinary Analysis (AMMA): An international research project and field campaign, *Bull. Am. Meteorol. Soc.*, *87*, 1739–1746, doi:10.1175/BAMS-87-12-1739.

Reid, J. S., and P. V. Hobbs (1998), Physical and optical properties of young smoke from individual biomass fires in Brazil, *J. Geophys. Res.*, *103*(D24), 32,013–32,030, doi:10.1029/98JD00159.

Remer, L. A., et al. (2005), The MODIS aerosol algorithm, products, and validation, *J. Atmos. Sci.*, *62*, 947–973, doi:10.1175/JAS3385.1.

Ross, J. L., P. V. Hobbs, and B. Holben (1998), Radiative characteristics of regional hazes dominated by smoke from biomass burning in Brazil: Closure tests and direct radiative forcing, *J. Geophys. Res.*, *103*(D24), 31,925–31,941, doi: 10.1029/97JD03677.

Roujean, J.-L., M. Leroy, and P.-Y. Deschamps (1992), A bidirectional reflectance model of the Earth's surface for the correction of remote sensing data, *J. Geophys. Res.*, *97*(D18), 20,455–20,468, doi:10.1029/92JD01411.

Rozanov, V. V., and A. A. Kokhanovsky (2005), On the molecular-aerosol coupling in remote sensing of aerosol from space, *IEEE Trans. Geosci. Remote Sens.*, *43*, 1536–1541, doi:10.1109/TGRS.2005.846859.

Rozanov, V. V., and A. A. Kokhanovsky (2006), The solution of the vector radiative transfer equation using the discrete ordinates technique: Selected applications, *Atmos. Res.*, *79*, 241–265, doi:10.1016/j.atmosres.2005.06.006.

Satheesh, S. K. (2002), Aerosol radiative forcing over land: Effect of surface and cloud reflection, *Ann. Geophys.*, *20*, 2105–2109.

Schmetz, J., P. Pili, S. Tjemkes, D. Just, J. Kerkmann, S. Rota, and A. Ratier (2002), An introduction to Meteosat Second Generation, *Bull. Am. Meteorol. Soc.*, *83*, 977–992, doi:10.1175/1520-0477(2002)083<0977:AITMSG>2.3.CO;2.

Seidel, F., D. Schläpfer, J. Nieke, and K. I. Itten (2008), Sensor performance requirements for the retrieval of atmospheric aerosols by airborne optical remote sensing, *Sensors*, *8*, 1901–1914, doi:10.3390/s8031901.

Sinyuk, A., et al. (2007), Simultaneous retrieval of aerosol and surface properties from a combination of AERONET and satellite data, *Remote Sens. Environ.*, *107*, 90–108, doi:10.1016/j.rse.2006.07.022.

Smirnov, A., B. N. Holben, T. F. Eck, O. Dubovik, and I. Slutsker (2000), Cloud screening and quality control algorithms for the AERONET database, *Remote Sens. Environ.*, *73*, 337–349, doi:10.1016/S0034-4257(00)00109-7.

Strahler, A. H., et al. (1999), MODIS BRDF/Albedo Product: Algorithm Theoretical Basis Document, version 5.0, 53 pp., NASA Goddard Space Flight Cent., Greenbelt, Md.

Sturm, B. (1981), Ocean color remote sensing and quantitative retrieval of surface chlorophyll in coastal waters using Nimbus CZCS data, in *Oceanography From Space*, edited by J. F. R. Gower, pp. 267–279, Plenum, New York.

Tanré, D., Y. Kaufman, T. Nakajima, and V. Ramanathan (2005), Preface to special section on Global Aerosol System, *J. Geophys. Res.*, *110*, D10S01, doi:10.1029/2004JD005724.

Toon, O. B., and T. P. Ackerman (1981), Algorithms for the calculation of scattering by stratified spheres, *Appl. Opt.*, *20*, 3657–3660, doi:10.1364/AO.20.003657.

Trentmann, J., B. Früh, O. Boucher, T. Trautmann, and M. O. Andreae (2003), Three-dimensional solar radiation effects on the actinic flux field in a biomass-burning plume, *J. Geophys. Res.*, *108*(D17), 4558, doi:10.1029/2003JD003422.

Trigo, I. F., et al. (2010), The satellite application facility on land surface analysis, *Int. J. Remote Sens.*, in press.

Vermote, E. F., D. Tanré, J. L. Deuzé, M. Herman, and J. J. Morcrette (1997), Second simulation of the satellite signal in the solar spectrum: An overview, *IEEE Trans. Geosci. Remote Sens.*, *35*, 675–686, doi:10.1109/36.581987.

Wang, M., K. D. Knobelspiesse, and C. R. McClain (2005), Study of the Sea-Viewing Wide Field-of-View Sensor (SeaWiFS) aerosol optical property data over ocean in combination with the ocean color products, *J. Geophys. Res.*, *110*, D10S06, doi:10.1029/2004JD004950.

Wanner, W., X. Li, and A. H. Strahler (1995), On the derivation of kernel-driven models of bidirectional reflectance, *J. Geophys. Res.*, *100*(D10), 21,077–21,090, doi:10.1029/95JD02371.

Wanner, W., A. H. Strahler, B. Hu, P. Lewis, J.-P. Muller, X. Li, C. L. B. Schaaf, and M. J. Barnsley (1997), Global retrieval of BRDF and albedo over land from EOS MODIS and MISR data: Theory and algorithm, *J. Geophys. Res.*, *102*(D14), 17,143–17,161, doi:10.1029/96JD03295.

Zhou, X., S. Li, and K. Stamnes (2003), Geometrical-optics code for computing the optical properties of large dielectric spheres, *Appl. Opt.*, *42*, 4295–4306, doi:10.1364/AO.42.004295.

D. Carrer, O. Hautecoeur, and J.-L. Roujean, GAME, CNRM, Météo-France, CNRS, 42, avenue Gaspard Coriolis, F-31057 Toulouse CEDEX, France. (dominique.carrer@meteo.fr)

T. Elias, LSCE, IPSL, L'Orme des Merisiers, F-91191 Gif-sur-Yvette, France.